Editors' Suggestion

Dynamical arrest in active nematic turbulence

Ido Lavi [1,2,*,†] Ricard Alert [2,3,4,5,6,7] Jean-François Joanny [8,9] and Jaume Casademunt [2,3]

[1]*Center for Computational Biology, Flatiron Institute, 162 5th Avenue, New York, New York 10010, USA*
[2]*Departament de Física de la Matèria Condensada, Universitat de Barcelona, Barcelona, Spain*
[3]*Universitat de Barcelona Institute of Complex Systems (UBICS), Barcelona, Spain*
[4]*Institució Catalana de Recerca i Estudis Avançats (ICREA), Barcelona, Spain*
[5]*Max Planck Institute for the Physics of Complex Systems, Nöthnitzerstrasse 38, 01187 Dresden, Germany*
[6]*Center for Systems Biology Dresden, Pfotenhauerstraße 108, 01307 Dresden, Germany*
[7]*Cluster of Excellence Physics of Life, TU Dresden, 01062 Dresden, Germany*
[8]*Collège de France, Paris, France*
[9]*Laboratoire PhysicoChimie Curie, Institut Curie, Université Paris Sciences & Lettres (PSL), Sorbonne Universités, Université Pierre et Marie Curie (UPMC), Paris, France*

(Received 12 November 2024; accepted 17 February 2026; published 17 March 2026)

Active fluids display spontaneous turbulentlike flows known as active turbulence. Recent work revealed that these flows have universal features, independent of the material properties and of the presence of topological defects. However, the differences between defect-laden and defect-free active turbulence remain largely unexplored. Here, by means of large-scale numerical simulations, we show that defect-free active nematic turbulence can undergo dynamical arrest. This state is characterized by an emergent network of nematic domain walls that channels coherent streams and suppresses chaotic flows. As the system evolves, the branched wall network produces a large-scale pattern with treelike topological properties. We find that flow alignment—the tendency of nematics to reorient under shear—enhances large-scale chaotic jets in contractile rodlike systems while promoting dynamical arrest in extensile systems. We further show that dynamical arrest arises regardless of whether defects are prohibited by construction or simply fail to form due to a high energy cost of defect cores. Taken together, our findings reveal a striking pattern-formation mechanism, with labyrinths emerging from active turbulence, and illuminate the rich transitional regime between defect-free and defect-laden dynamics. These behaviors call for the experimental realization of active nematics at vanishing or low defect densities, and underscore that, in extensile rodlike nematics, topological defects enable turbulence by preventing dynamical arrest.

DOI: 10.1103/1jyc-t1z4

I. INTRODUCTION

Active fluids are driven internally by their own components—be they molecular motors, cells, or synthetic colloidal particles. This internal driving produces spontaneous flows, which often exhibit spatiotemporal chaos at high activity [1]. Chaotic flows have been observed in a variety of systems, such as bacterial suspensions [2–11], sperm [12], mixtures of cytoskeletal components [13–22], cell monolayers [23–27], and artificial self-propelled particles [28–31]. Although all these systems operate at low Reynolds number, for which inertia is negligible, the flows are reminiscent of classic inertial turbulence. Hence, active chaotic flows are generically referred to as active turbulence [1].

Active turbulence encompasses systems with different symmetries, including polar or nematic orientational order, each exhibiting unique statistical properties [1]. Recent work showed that the velocity power spectrum of active nematic turbulence features scaling laws with universal exponents independent of the material properties of the fluid such as its viscosity and activity [22,32,33]. In particular, the q^{-1} scaling of the velocity power spectrum at small wave numbers q was shown to be highly robust in simulations, provided the Reynolds number remains low [34]. Whereas the -1 exponent was first predicted for defect-laden dynamics [32], turbulence with the same universal exponent was also found for strongly ordered nematics in the absence of defects [33]. However, how the material properties and the presence or absence of defects affect other, nonuniversal features of the flow field remains unclear.

Here, we show that defect-free active nematic turbulence exhibits arrested patterns not seen in the presence of defects. We reveal these patterns by studying the effect of the flow-alignment parameter ν, which characterizes the tendency of liquid crystals to reorient under shear. As expected, we find that the scaling exponent of the velocity power spectrum is unaffected when varying ν, confirming its universal character

*Contact author: ilavi@flatironinstitute.org
†Present address: Flatiron Institute, New York, New York, USA.

[1,33]. Despite keeping the same scaling, we find that flow alignment strongly affects both the strength and the spatiotemporal structure of the flows.

In the absence of defects, we identify two distinct regimes depending on the parameter combination $\mathrm{sign}(\zeta)\nu$, where ζ is the active stress parameter, with $\zeta > 0$ for extensile and $\zeta < 0$ for contractile stresses, respectively. We discuss the case of rodlike nematic components, for which $\nu \leqslant 0$. In the flow-aligning regime, where $\nu < -1$, we find that contractile nematics (with $\zeta\nu > 0$) exhibit strongly chaotic flows and nematic distortions, which largely decorrelate from one another. In this regime, nematic domain walls—lines of strong variation of the director—appear, split, and dissolve, forming a dynamically reorganizing pattern [Figs. 1(a)–1(c) and Movie S1 of the Supplemental Material [35]]. In contrast, for extensile aligning nematics ($\zeta\nu < 0$), we find that domain walls are strongly stabilized by the flow they entrain. The walls typically grow and branch but neither break nor merge. As walls avoid each other, they become arrested (or gridlocked) in a space-filling treelike pattern [Figs. 1(d)–1(f) and Movie S2 of the Supplemental Material [35]]. Once arrested, the pattern exhibits slow residual dynamics that shares some features with ageing phenomena in glassy systems. The special case $\nu = 0$ has been the focus of previous work [33] and is considered here as a reference. The dynamics in this case lie between these two extremes while also manifesting comparatively shorter wavelengths (Fig. S1 and Movie S3 of the Supplemental Material [35]).

We uncover that the dynamical arrest stems from the emergence of an effective topology, characterized by a set of connectivity rules for the domain walls imposed by the combined effects of activity and flow alignment. In particular, we demonstrate that, in the absence of topological defects, the arrested state is organized by local nematic structures, which we name pseudodefects. We discuss their topological interpretation and demonstrate that they coexist with actual defects in experiments on microtubule-based active nematics.

Finally, we show that dynamical arrest is not exclusive to our minimal defect-free model, but rather a robust phenomenon that also arises in the full Q-tensor formulation of active nematics. In this more general framework, an additional control parameter—the defect core size—governs whether topological defects are energetically suppressed or favored. By tuning this parameter, we uncover a transition in which defect nucleation ramps up sharply near a threshold. As defects proliferate, the flow crosses over from a dynamically arrested state, organized into streams that are channeled through the wall network, to the more familiar regime of chaotic, vortex-dominated flows. These simulations further highlight the role of defects in enabling active turbulence and reveal a rich transitional regime where defects and domain walls can coexist.

II. DIRECTOR-BASED DEFECT-FREE MODEL

We generalize our previous minimal model of active nematic turbulence [33] by adding flow alignment and the Ericksen stress [36]. This yields the active Ericksen-Leslie liquid crystal model, widely regarded as a paradigm in this field [1].

We work at vanishing Reynolds number, for which momentum balance reads

$$0 = -\partial_\alpha P + \partial_\beta\left(\sigma^{\mathrm{a}}_{\alpha\beta} + \sigma^{\mathrm{E}}_{\alpha\beta} + \sigma_{\alpha\beta}\right). \tag{1}$$

The pressure P enforces the incompressibility condition $\partial_\alpha v_\alpha = 0$ of the flow field $\boldsymbol{v}$. The next two terms are the divergence of the antisymmetric part of the stress tensor and of the symmetric Ericksen stress, respectively [36,37]:

$$\sigma^{\mathrm{a}}_{\alpha\beta} = \frac{1}{2}(n_\alpha h_\beta - h_\alpha n_\beta), \quad \sigma^{\mathrm{E}}_{\alpha\beta} = -\frac{\delta F_n}{\delta(\partial_\alpha n_\gamma)}\partial_\beta n_\gamma. \tag{2}$$

These stresses arise from the elastic distortions of the director field $\boldsymbol{n}$. Distortions produce an orientational field $h_\alpha = -\delta F_n/\delta n_\alpha = K\nabla^2 n_\alpha + h^0_\parallel n_\alpha$ computed from the Frank free energy, which, in the one-constant K approximation, reads

$$F_n = \int\left[\frac{K}{2}(\partial_\alpha n_\beta)(\partial_\alpha n_\beta) - \frac{1}{2}h^0_\parallel n_\alpha n_\alpha\right]\mathrm{d}^2\boldsymbol{r}. \tag{3}$$

Here, we assumed that the fluid is deep in the nematic phase so that the director field has a fixed modulus $|\boldsymbol{n}| = 1$. This constraint is imposed by the second term through the Lagrange multiplier $h^0_\parallel$. We start with a continuous director field, which precludes the generation of topological defects [33,38]. Note that this constraint is lifted in our analysis of the full Q-tensor model, presented in the final section of this paper.

The last term in Eq. (1) arises from the symmetric part of the deviatoric stress, which is given by the constitutive equation [37,39–41]

$$\sigma_{\alpha\beta} = 2\eta v_{\alpha\beta} - \zeta\hat{q}_{\alpha\beta} + \frac{\nu}{2}(n_\alpha h_\beta + h_\alpha n_\beta - n_\gamma h_\gamma \delta_{\alpha\beta}). \tag{4}$$

Here, η is the shear viscosity, $v_{\alpha\beta} = 1/2(\partial_\alpha v_\beta + \partial_\beta v_\alpha)$ is the symmetric part of the strain-rate tensor, ζ is the active stress parameter, and $\hat{q}_{\alpha\beta} = n_\alpha n_\beta - 1/2\,\delta_{\alpha\beta}$ is the nematic orientation tensor defined by the director $\boldsymbol{n}$. The last term describes stresses due to flow alignment, with parameter ν.

As in passive nematics, the dynamics of the director field are given by

$$\partial_t n_\alpha + v_\beta\partial_\beta n_\alpha + \omega_{\alpha\beta}n_\beta = \frac{1}{\gamma}h_\alpha - \nu v_{\alpha\beta}n_\beta, \tag{5}$$

where $\omega_{\alpha\beta} = 1/2(\partial_\alpha v_\beta - \partial_\beta v_\alpha)$ is the vorticity tensor and γ is the rotational viscosity. The left-hand side (LHS) is the corotational material derivative of the director field. On the right-hand side (RHS), the orientational field h_α specifies the elastic torque acting on the director, whereas the last term captures its reorientation due to extensional flow, i.e., the flow-alignment effect.

Nondimensionalizing the equations, we rescale length by the system size L, time by the active time $\tau_{\mathrm{a}} = \eta/|\zeta|$, pressure by the active stress $|\zeta|$, and orientational field by K/L^2. To eliminate the pressure, we take the curl of Eq. (1) and obtain a Poisson equation for the vorticity ω, which we write in terms of the stream function ψ (defined by $v_x = \partial_y\psi$ and $v_y = -\partial_x\psi$) [38], as $\omega = -\nabla^2\psi$:

$$\nabla^2\omega = -\nabla^4\psi = -S\partial_\alpha\partial_\beta\bar{q}_{\alpha\beta} + R\nu\partial_\alpha\partial_\beta(\bar{q}_{\alpha\beta}h_\parallel - \hat{q}_{\alpha\beta}h_\perp) + \frac{R}{2}\nabla^2 h_\perp + R\epsilon_{\alpha\beta}(\partial_\alpha h_\perp)\partial_\beta\theta. \tag{6}$$

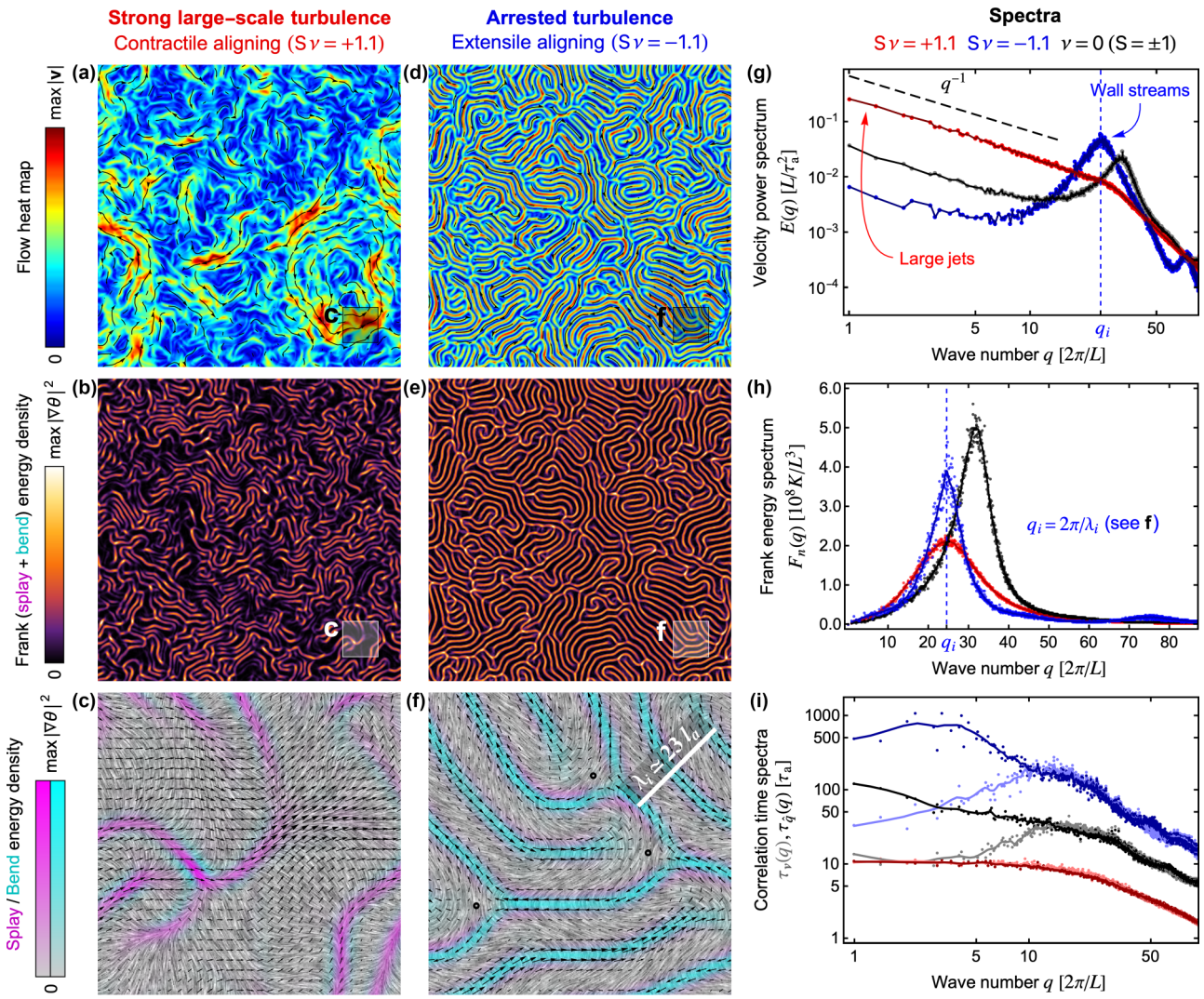

FIG. 1. Strong and arrested regimes of active nematic turbulence. Snapshots from simulations of defect-free active nematic turbulence in contractile [panels (a)–(c)] and extensile [panels (d)–(f)] flow-aligning systems. Parameter values were set to $R = 1$, $\nu = -1.1$, and $A = 3.2 \times 10^5$. Top panels (a) and (d) show the flow field; black curves are streamlines, and the color indicates the speed (see Movies S1 and S2 of the Supplemental Material [35]). Middle panels (b) and (e) show the Frank free energy density $\sim|\nabla\theta|^2$, with high-intensity lines corresponding to nematic domain walls (see Movies S1 and S2 of the Supplemental Material [35]). Bottom panels (c) and (f) are zooms highlighting the type of nematic distortion as well as the interplay between nematic walls and flows. The gray-scale background is the line integral convolution representation of the director field $\boldsymbol{n}$. Magenta and cyan intensities, respectively, represent splay $(\nabla \cdot \boldsymbol{n})^2$ and bend $|\nabla \times \boldsymbol{n}|^2$ contributions to the Frank energy density. The black arrows represent the flow field $\boldsymbol{v}$, which localizes along the nematic walls in the arrested regime. Black circles indicate stagnation points of the flow. White scale bar represents the selected wavelength λ_i. (g)–(i) Spectra characterizing fully developed active nematic turbulence (see details in Appendix B). The lines in panels (h) and (i) represent a smoothed (Gaussian) interpolation of the computed data points. We compare the flow-aligning contractile [red, as in panels (a)–(c) and Movie S1 of the Supplemental Material [35]] and extensile [blue, as in panels (d)–(f) and Movie S2 of the Supplemental Material [35]] cases with the $\nu = 0$ case (black, as in Fig. S1 and Movie S3 of the Supplemental Material [35]), for which contractile and extensile stresses are equivalent up to a rotation [38,42,43]. (g) Velocity power spectrum on a log-log scale, showing (1) the universal low-q scaling law and (2) the distinct organization of flows across scales in the different cases. The wider scaling regime in the contractile case captures the strong large-scale jets [see panel (a)]. The peak in the extensile case is representative of wall streams [see panel (d)]. (h) Frank energy spectrum, showing that (1) the selected wavelength (peak position) depends on ν but not on the sign of active stress and (2) the peak width depends on the sign of active stress when $\nu \neq 0$. (i) Spectrum of correlation times associated with the flow $\boldsymbol{v}$ (light colored points and lines) and the nematic tensor $\hat{q}_{\alpha\beta}$ (darker points and lines). This log-log plot reveals strong differences in decay times between the regimes, as well as the differences between the flow and nematic tensor within a regime. Correlation times are extracted from exponential fits to the corresponding space-time autocorrelation functions in Fourier space (see Appendix B).

Here, S is the sign of the active stresses, with $S = \pm 1$ for extensile and contractile stresses, respectively, and θ is the nematic director angle: $\boldsymbol{n} = (\cos\theta, \sin\theta)$. The right-hand side contains four sources of vorticity, arising respectively from active, flow-alignment, antisymmetric, and Ericksen stresses. We used the totally antisymmetric tensor $\epsilon_{\alpha\beta}$ to define $\bar{q}_{\alpha\beta} \equiv -\epsilon_{\alpha\gamma}\hat{q}_{\gamma\beta}$. We also introduced the parallel and perpendicular components of the orientational field [38]:

$$h_\perp = \frac{1}{A}\nabla^2\theta, \quad h_\parallel = \nu\bar{q}_{\alpha\beta}\partial_\alpha\partial_\beta\psi. \tag{7}$$

Equations (6) and (7) contain three dimensionless parameters: the activity number $A = L^2/\ell_a^2$, the viscosity ratio $R = \gamma/\eta$, and the flow-alignment parameter ν. The activity number compares the system size L with the active length $\ell_a = \sqrt{K/(|\zeta|R)}$ defined by the balance between active and elastic nematic stresses.

Finally, the director dynamics [Eq. (5)] breaks down into a component parallel to $\boldsymbol{n}$, which specifies $h_\parallel$ as given in Eq. (7), and a component perpendicular to $\boldsymbol{n}$, which determines the dynamics of the nematic angle θ [38]:

$$\partial_t\theta - \epsilon_{\alpha\beta}\partial_\alpha\psi\,\partial_\beta\theta + \tfrac{1}{2}\nabla^2\psi = h_\perp + \nu\hat{q}_{\alpha\beta}\partial_\alpha\partial_\beta\psi. \tag{8}$$

Equations (6)–(8) give the hydrodynamics of our active fluid in terms of two fields: the angle θ and the stream function ψ.

We numerically integrate Eqs. (6)–(8) in a square with periodic boundary conditions using a hybrid numerical scheme that combines a pseudospectral method for Eq. (6) with the finite-element method for Eq. (8) (Appendix A). Unless otherwise specified, we set $R = 1$ and $A = 3.2 \times 10^5$, for which the system was shown to develop large-scale active turbulence when $\nu = 0$ [33]. The dynamics are invariant under the transformation ($\nu \to -\nu$, $S \to -S$, $\theta \to \theta \pm \pi/2$), meaning that changing the signs of ν and S simultaneously leaves the system invariant up to a rotation [38,42,43].

III. REGIMES OF DEFECT-FREE ACTIVE TURBULENCE

A. Strong large-scale turbulence

We first study the case $S\nu > 1$, realized with contractile flow-aligning rods ($S = -1$ and $\nu = -1.1$). We find a chaotic flow field with vortices at many scales and strong (albeit transient) large-scale jets [Fig. 1(a)]. These flow patterns stem from long-range hydrodynamic interactions and appear to be locally uncorrelated with the distortion pattern of the director field [Fig. 1(c)], which also evolves chaotically. The Frank energy density concentrates along domain walls [Figs. 1(b) and 1(c)]—well-known regions of strong orientation gradients [44–46]. Such walls feature a typical separation length, corresponding to the peak position in the Frank energy spectrum [Fig. 1(h), red], coinciding with the peak of the nematic tensor power spectrum (Fig. 9, red). Compared with the $\nu = 0$ case [33], the nematic pattern in the $S\nu > 1$ regime appears more broken, with fragmented walls coexisting with wall-free regions [dark patches in Fig. 1(b)]. As a consequence, the total Frank free energy is smaller, and its peak is shifted to larger scales [Fig. 1(h), red]. A dynamically rearranging pattern emerges as walls spontaneously appear, split, and dissolve (Movie S1 and left panel of Movie S4 of the Supplemental Material [35]). Both the flows and the nematic tensor are very dynamic, as confirmed by their short correlation time at all length scales [Fig. 1(i), red].

In recent work, we have shown that, for $S\nu > 1$, both the quiescent state with uniform orientation and the flowing state with splaying domain walls are nonlinearly unstable against one-dimensional (1D) modulations [38]. Thus, strong enough perturbations can trigger sudden transitions between these states. For this reason, we assert that domain wall patterns can be disrupted by the strong turbulent flows. In the two-dimensional (2D) simulations shown here, we observe the coexistence of uniform and wall-laden patches that continuously rearrange. We conclude that the metastability associated with this regime strongly enhances the chaotic flows, particularly at large scales, as indicated by the wide q^{-1} scaling regime in Fig. 1(g), red.

B. Arrested turbulence

We now study the case $S\nu < -1$, realized with extensile flow-aligning rods ($S = +1$ and $\nu = -1.1$). While the system still evolves chaotically, large-scale flows are much weaker than in the other cases, with the q^{-1} power law spanning a narrower range of scales [Fig. 1(g), blue]. Rather than large-scale jets, the dominant flows are at shorter length scales, as indicated by the enhanced peak of the velocity power spectrum [Fig. 1(g), blue]. These smaller-scale flows form streams that are strongly localized along the bending domain walls where the active stress gradients are larger [Figs. 1(d)–1(f)].

In contrast to the nonarrested case, here a connected wall pattern extends across the entire system [Fig. 1(e)]. The Frank free energy spectrum is more narrowly peaked at the characteristic length scale [Fig. 1(h), blue], compared to the nonarrested case [Fig. 1(h), red]. The same peak is also prominent in the nematic tensor power spectrum (Fig. 9, blue). Strikingly, the nematic wall pattern becomes far less dynamic; the walls and their associated streams become locked in a treelike pattern. We term this phenomenon dynamical arrest. The weak large-scale chaotic flows make the pattern fluctuate only slightly (Movie S2 and right panel of Movie S4 of the Supplemental Material [35]). The dynamical arrest manifests in much longer correlation times, especially of the nematic tensor field at large scales [Fig. 1(i), blue]. The treelike pattern of domain walls is characterized by unique connectivity properties, which we elaborate on later. We conclude that, in the absence of topological defects, the combined effects of extensile stress and rodlike flow alignment give rise to the arrest of active nematic turbulence.

To understand the mechanism of arrest, we note that the spontaneous-flow instability, which ultimately drives turbulence, generates shear flow [47]. This shear produces antiparallel flows that concentrate along the nematic walls [33,38,42,43,47,48]. The walls are directed lines, with their direction defined by the vector $(\partial_y\theta, -\partial_x\theta)$, which is perpendicular to the gradient of the angle and coincides with the flow direction in the arrested regime.

Quasi one-dimensional wall patterns tend to coarsen, leading to larger domains [Fig. 2(a) and right panel of Movie S4 of the Supplemental Material [35]]. Since the director orientation is roughly uniform within such domains, the same instability prompts distortions in a perpendicular direction

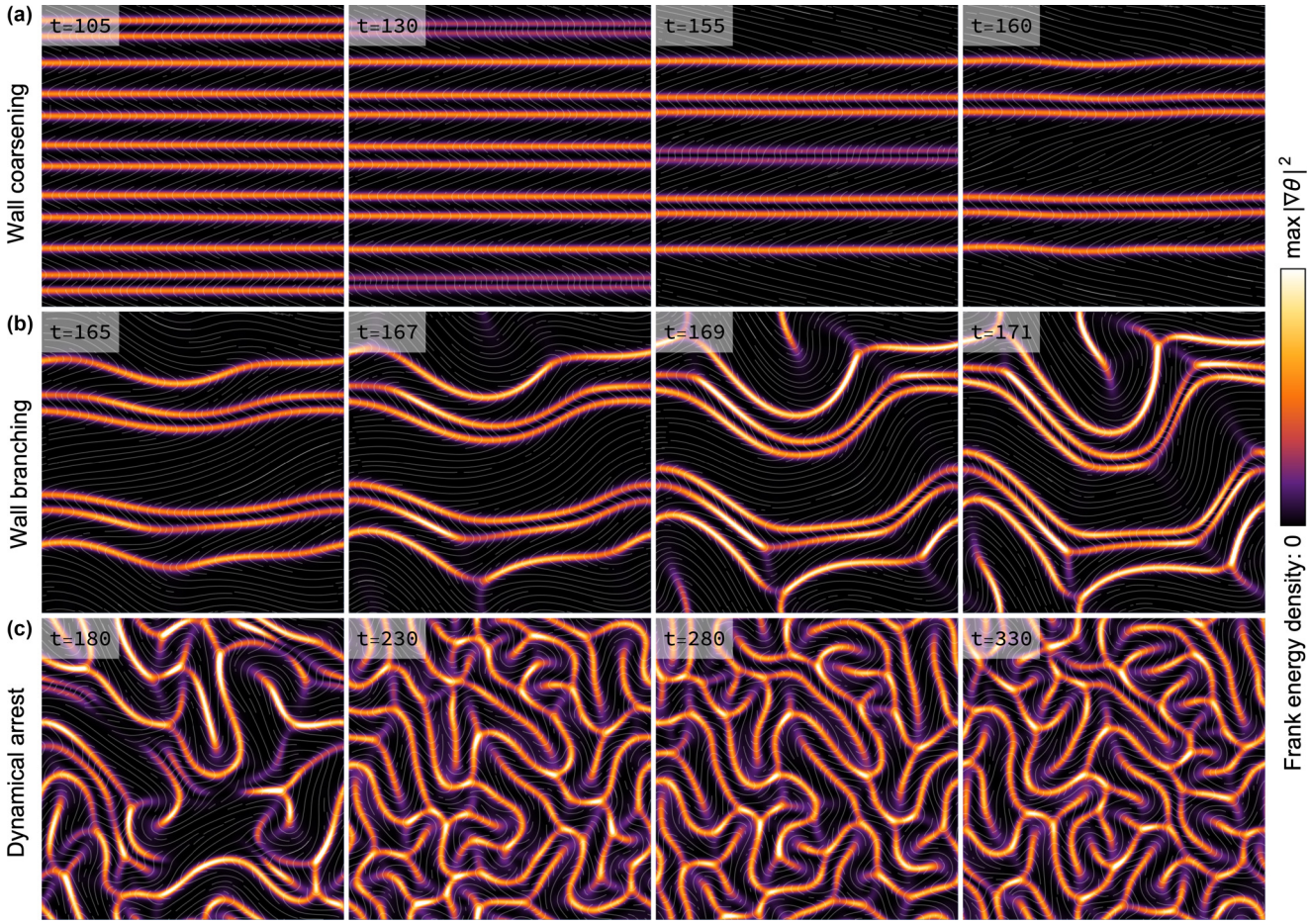

FIG. 2. Wall coarsening, branching, and dynamical arrest. Sequential snapshots from a single simulation in the extensile flow-aligning regime, showing the coarsening of bending walls [panel (a), top row], the zigzag instability of the coarsened configuration, followed by wall branching and rapid tip growth [panel (b), second row], and the evolution toward the arrested tree pattern [panel (c), bottom row]. The initial condition was set to a striped pattern of wavelength that matches the typical length selected in the chaotic regime (see first and final panels). A perturbation along the y axis triggers the coarsening of one-dimensional stripes, confirming that straight antiparallel walls do not have a preferred separation. The length selected in the treelike pattern is determined by two-dimensional interactions, with growing branches avoiding preexisting walls. Parameter values are $R = 1$, $S = 1$, $\nu = -1.1$, and $A = 19\,692$ (chosen so that the system size roughly equals six times the selected wavelength).

[33,48]. This process induces sequential "zigzag" instabilities, leading to wall branching and progressively smaller domains, until a characteristic wavelength is selected [Fig. 2(b) and right panel of Movie S4 of the Supplemental Material [35]], [19,33]. When an open end of a branch approaches another wall perpendicularly, it is deflected and becomes antiparallel to that wall. The growth of branches typically stops when they are blocked by a preexisting branch point. Ultimately, these dynamics lead to a gridlocked pattern [Fig. 2(c) and right panel of Movie S4 of the Supplemental Material [35]].

When a growing open-ended wall encounters a branch point ahead of it, the outflowing stream at the end point of that wall is diverted symmetrically in perpendicular directions so that material can join the streams of the two walls that split away from the branch point [see Fig. 1(f), around the black circles]. In effect, this diversion creates a local stagnation point: Flows arrive from the direction of the open-ended wall and depart in the perpendicular direction, which is also the direction to which rods tend to align by flow alignment. For bend walls—generated by an extensile stress—the director along the incident wall is perpendicular to the wall itself, and thus naturally aligned with the extensional axis of the flow at the stagnation point. We therefore propose that the structure around the stagnation point acts as a trap, and its stability is central to understanding how flow alignment promotes the dynamical arrest of active turbulence.

IV. PSEUDOTOPOLOGY OF DOMAIN WALL NETWORKS

A. Wall nodes define pseudodefects

The domain walls emerging in our system are typically of a single type [either splaying or bending; see Figs. 1(c) and 1(f)]. Such walls generically feature three types of nodes:

(1) Startpoints, with one outgoing wall and no incoming wall [Fig. 3(a)].

(2) Branchpoints, with one incoming wall and two outgoing walls [Fig. 3(b)].

(3) Endpoints, with one incoming wall and no outgoing wall [Fig. 3(c)].

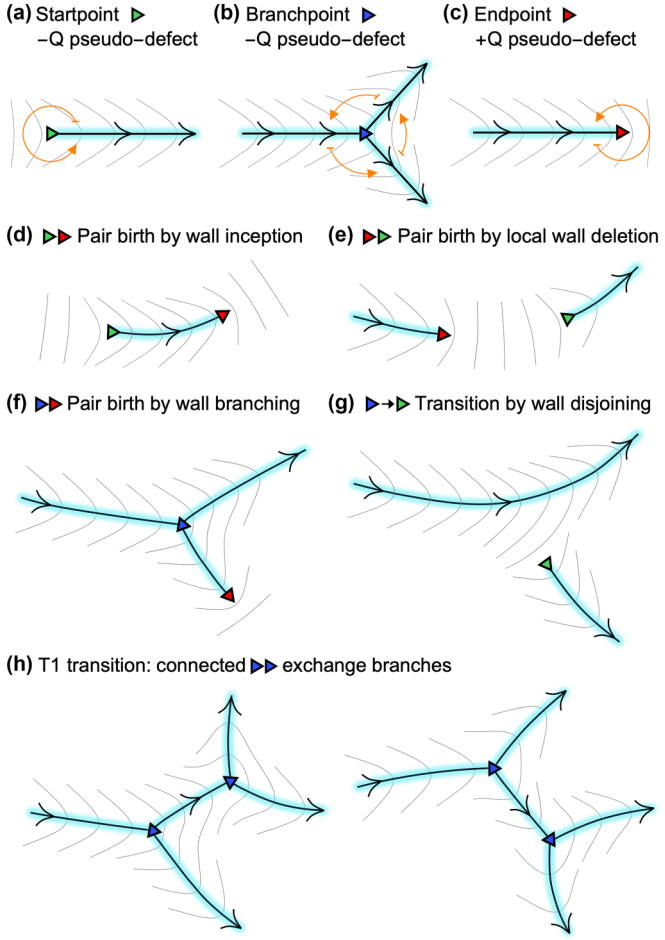

FIG. 3. Domain wall nodes and their pseudotopology. In all diagrams, black directed lines represent nematic bending walls, with gray lines tracing the director and cyan indicating the bending energy. (a)–(c) Nodes are either startpoints (green, negative pseudodefects), branchpoints (blue, negative pseudodefects), or endpoints (red, positive pseudodefects). The orange curves illustrate the paths excluding walls used to define the pseudocharge (Appendix C). (d)–(e) Two ways in which a startpoint-endpoint pair of opposite charge can be born. The inverse processes of (d) [complete wall dissolution] and (e) [local wall completion] result in the annihilation of such pairs. (f) Wall branching gives birth to a branchpoint-endpoint pair, also of opposite charge. A connected pair may annihilate via branch retraction. (g) A branchpoint [panel (b)] transitions into a startpoint when one outgoing wall disjoins. The inverse process corresponds to a startpoint [panel (a)] joining with a bare wall. (h) Connected branchpoints can shrink their connecting branch, transiently creating a $-2Q$ pseudocharged structure, exchange outgoing walls, and extend again in the perpendicular direction. The processes depicted in panels (d)–(h) are further illustrated in Animations S1–S5 of the Supplemental Material [35].

These recurring node structures arise naturally in our simulations and serve as an effective framework for characterizing defect-free dynamics. We note that a node with two incoming walls and one outgoing wall (a mergepoint) is only possible by combining different wall types (Fig. S2 of the Supplemental Material [35]). Additionally, we observe that startpoints are very common in the nonarrested (contractile aligning) regime but become increasingly rare over time in the arrested (extensile aligning) regime.

We define these three types of nodes as pseudodefects. Unlike proper topological defects, they are not phase singularities of the director field and do not carry a topological charge. Nevertheless, the director varies around them in a manner that resembles true nematic defects, except for its sharp counter variation across the walls. We thus assign the nodes a pseudocharge, defined as the number of turns of the director along a path that surrounds the pseudodefect, excluding the sharp variation across all intersecting walls [Figs. 3(a)–3(c)]. The excluded walls in this definition are analogous to the so-called Dirac strings, which are constructs that enable magnetic monopoles in Maxwell's equations [49] (see discussion in Appendix C). With this definition, endpoints have a positive pseudocharge $+Q$ [Fig. 3(c)] and both startpoints and branchpoints have pseudocharge $-Q$ [Figs. 3(a) and 3(b)]. The pseudocharge depends on ν. For $S\nu > -1$, we have $Q \simeq 1/2$, while for $S\nu \leqslant -1$, we have $Q \simeq \frac{1}{2}[1 - \frac{1}{\pi}\arccos(|\nu|^{-1})]$ (see details in Appendix C). The total pseudocharge contained in a closed domain is mQ, where m is the difference between the number of walls crossing the path inward and outward (Appendix C). All pseudodefects have polarity, defined by the direction of the outgoing wall for startpoints [Fig. 3(a)] and the direction of the incoming wall for branchpoints and endpoints [Figs. 3(b) and 3(c)].

The topological pseudocharge is preserved by the dynamics of the director. Pseudodefects with opposite charges are created in pairs and annihilated in pairs [Figs. 3(d)–3(f) and Animations S1–S3 of the Supplemental Material [35]], similarly to actual nematic defects. A wall endpoint cannot merge with a preexisting wall. Instead, it can connect with a startpoint ahead of it [the inverse process of Fig. 3(e) and Animation S2 of the Supplemental Material [35]] or, through wall shrinkage, it can annihilate with the nearest negative pseudodefect it is *connected to* [the inverse processes of Figs. 3(d) and 3(f) and Animations S1 and S3 of the Supplemental Material [35]]. Notably, this nearest connected point does not need to be its birth pair and may be quite a long distance away, as we often observe in the arrested regime. In addition to pair birth and annihilation, negative pseudodefects can transition from one to the other while conserving the pseudocharge [Fig. 3(g) and its inverse process and Animation S4 of the Supplemental Material [35]]. In another pseudotopological transition, connected branchpoints can exchange branches [Fig. 3(h) and Animation S5 of the Supplemental Material [35]]. This process is akin to a T1 transition in foams and tissues, except that our lines are directed, and branching nodes are restricted to having one incoming wall and two outgoing walls. As a result, T2 transitions are not possible.

One can imagine other transitions between wall nodes that are permitted by the pseudotopological rules. To the best of our understanding, such processes can be viewed as either analogues or sequences of the basic transitions shown in Fig. 3. Moreover, all processes involving startpoints are rare in arrested wall networks.

B. Network motifs

In the arrested turbulence regime (extensile rods with $S\nu <$ 0), the processes of wall folding, branching, extension, and

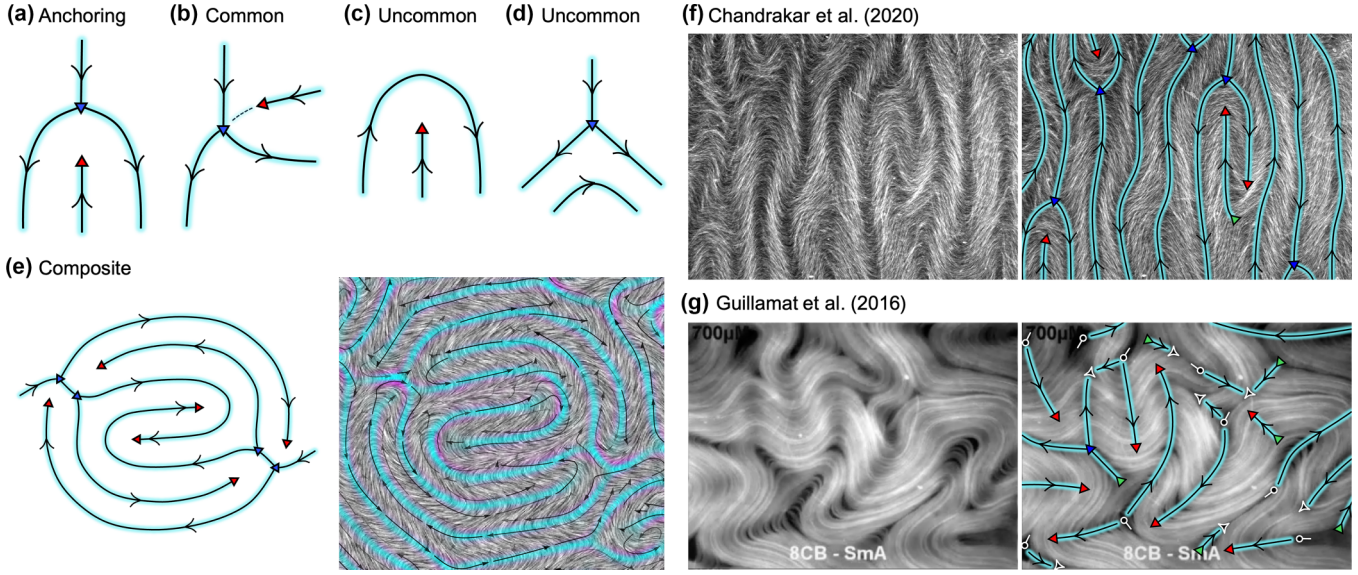

FIG. 4. Motifs of arrested wall networks and experimental snapshots of microtubule-kinesin active nematics. In all diagrams, lines, nodes, and colors are as defined in Fig. 3. (a)–(d) Basic network motifs. The anchoring motif [panel (a)] is made of an endpoint and branchpoint that meet head-on, with the endpoint trapped between the two outgoing walls of the branchpoint. In the motif depicted in panel (b), the endpoint meets the branchpoint from one of its sides, i.e., between the incoming wall and an outgoing wall. The dashed line traces a weak distortion, indicating that the wall associated with the endpoint tends to align its direction with the outgoing wall on the opposite side of the branchpoint. The motifs shown in panels (c) and (d) involve a single pseudodefect interacting with a bare wall. These, along with panel (b), do not follow the tendency to have strictly antiparallel walls. (e) Composite motif schematic (left) and one formed spontaneously in a simulation (right). The stream plot on the right represents the flow, with black indicating maximal $|\boldsymbol{v}|$ and full transparency indicating $|\boldsymbol{v}| = 0$. The gray background is the line-integral-convolution representation of the nematic director $\boldsymbol{n}$. Parameter values and color legend for splay and bend distortions are as in Fig. 1(f). (f), (g) Raw fluorescence images from experiments (left panels) and overlaid schematic drawings (right panels) depicting domain walls, pseudodefects, and actual $\pm 1/2$ defects in white. (f) Taken from a movie in Ref. [50] (courtesy of Guillaume Duclos), which shows the evolution of the microtubule-based nematic following the bending instability of the aligned state. (g) Taken from a movie in Ref. [51] (courtesy of Pau Guillamat), which shows a turbulent transient with all types of pseudodefects and actual nematic defects. Note how walls may also originate from true $+1/2$ defects and be absorbed by true $-1/2$ defects.

arrest produce a directed treelike network of self-avoiding walls (Fig. 2). This network does not form closed loops in a simply connected domain because such a loop would enclose a topological charge of 1, implying actual nematic defects, which our system forbids.

We find that endpoints propagate rapidly in the direction of their polarity, until they are blocked by other walls. Startpoints, on the other hand, move quickly in the opposite direction of their polarity until their wall dissolves or they merge with another wall, transitioning into a branchpoint. Unlike endpoints and startpoints, branchpoints do not move in the direction parallel or antiparallel to their polarity. Rather, when they are created [Fig. 3(f)], they tend to deflect only slightly in the direction of the newly formed branch [Fig. 2(b)]. Hence, in the sense of their mobility, endpoints are akin to actual $+1/2$ nematic defects and branchpoints are similar to $-1/2$ defects, which are not mobile. Despite these similarities, we emphasize that actual defects generate fundamentally different dynamics, likely due to fewer constraints on their mobility and the transitions they can undergo. This contrast becomes evident in the final section, where we perform full Q-tensor simulations that permit the nucleation of true topological defects.

Ultimately, the pseudodefects—primarily endpoints and branchpoints (in arrested states)—maintain a steady distance from neighboring walls and organize into motifs like those shown in Figs. 4(a)–4(d). A frequent motif, which we call the anchoring motif [Fig. 4(a)], is the one discussed previously in relation to the stagnation points in Fig. 1(f). We postulate that this structure might be particularly stable because neighboring walls are antiparallel, as promoted by the spontaneous-flow instability. In contrast, the other basic motifs [Figs. 4(b)–4(d)] feature some neighboring walls that are parallel. For large system sizes, a variety of composite structures combining all types of motifs can emerge and persist for long times (see Movie S2 of the Supplemental Material [35]). One such structure is shown in Fig. 4(e).

We identified bending domain walls, pseudodefects, and our motifs in images and videos of microtubule-based active nematics [15,50–54] [Figs. 4(f) and 4(g)]. In Fig. 4(f), the spontaneous-flow instability leads to the growth of bending domain walls and the emergence of pseudodefects. These tend to organize in interlaced anchoring motifs, which are also frequently observed in our simulations. In Fig. 4(g), pseudodefects are seen to coexist with actual nematic defects (white). Since the latter may also act as origin points or termination points of walls, there may be an interesting interplay between both types of structures in organizing the dynamics of the system. We take initial steps toward exploring this interaction in the final section, where we analyze the full Q-tensor model. We further note that a very recent study [54] observed that a series of folding events generates an extensive network of

bending domain walls, where both types of nodes (pseudodefects and true defects) are clearly present. Importantly, in these experimental examples, the system does not maintain an arrested state. We expand on this aspect further in the final discussion.

C. Ageing dynamics

The dynamics of active nematics are not relaxational, and the arrested patterns emerging in the extensile case coexist with a background of weak large-scale chaotic flows. Nevertheless, these dynamics share interesting similarities with relaxational systems that exhibit frustration. In particular, trapping motifs [Figs. 4(a) and 4(b)] might promote arrest similarly to how cages and locally favored structures promote arrest in gels and glasses [55–57]. After an initial transient in which sequential branching establishes the network, we find that the wall network undergoes a slow relaxation that is reminiscent of the ageing of gels and glasses. The background turbulentlike flows produce small low-q fluctuations that slowly evolve the pattern. This includes jittering the walls and inducing some pseudotopological transitions in the network; primarily those depicted in Figs. 3(f)–3(h) and their inverse processes. Crucially, these represent a highly restrictive subset of transitions compared to the full range of processes enabled when startpoints are more prominently present. Through this fluctuating process, we find that the number of pseudodefects gradually decreases (Fig. 5 and Movie S5 of the Supplemental Material [35]), mostly via annihilation of connected branchpoint-endpoint pairs. As some walls shrink and disappear from the network, others extend, thereby maintaining the selected wavelength. At long times ($\sim 10^3 \tau_a$), the evolution slows down, and the number of pseudodefects seems to approach a steady state [Fig. 5(c)]. This relaxation occurs on timescales of hundreds of τ_a and appears to be a specific feature of arrested wall networks. It is absent in the contractile aligning regime, and in the presence of true topological defects—as shown in the final section.

D. Unicursal labyrinths

When there are no startpoints, which is typical in the extensile aligning regime, the *gaps between the walls* form unicursal labyrinths of a type known as meanders, defined by having a single path with neither bifurcations nor dead ends. A typical wall network encloses a small and even number of such labyrinths, with each one closing on itself through the periodic boundaries, i.e., through the hole of the torus, which is not a simply connected domain [Figs. 6(a) and 6(b)]. On the other hand, the wall network bounding these unicursal paths forms a maze, defined as having multiple bifurcations and dead ends, corresponding to our branchpoints and endpoints. The specific walls separating the *different* unicursal labyrinths are initially generated by the spontaneous-flow instability. There are as many of these *primary walls* as there are unicursal labyrinths, and they also close on themselves through the periodic boundaries. Since primary walls are the only paths on the network that avoid dead ends, they can be thought of as the solutions to the maze.

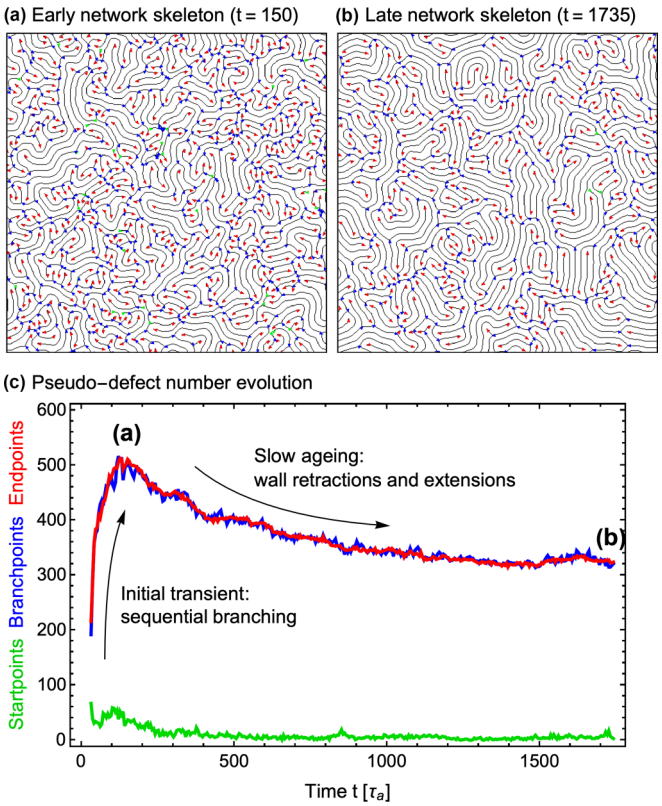

FIG. 5. Ageing of the arrested wall network. Skeleton of the domain walls (black) with startpoints, branchpoints, and endpoints (green, blue, and red triangular nodes) at an early time [panel (a)] and a late time [panel (b)]. The detection of the network skeleton and its nodes is described in Appendix E (Fig. 13). (c) Evolution of the number of startpoints (green), branchpoints (blue), and endpoints (red). In the initial transient, sequential "zigzag" instabilities result in the proliferation of both branchpoints and endpoints. Once the wall pattern establishes a wavelength, the system ages slowly as some endpoints retract and annihilate with their connected branchpoint, while others extend (Movie S5 of the Supplemental Material [35]). Throughout the simulation, there are frequent transitions between branchpoints and startpoints, though the number of startpoints remains low. Additionally, the detection algorithm is not perfect, occasionally misidentifying endpoints or branchpoints as startpoints and vice versa. Parameter values were set to $R = 1, S = 1, \nu = -0.9$, and $A = 3.2 \times 10^5$.

Paintings, rock carvings, ornaments, and monuments depicting unicursal labyrinths predate recorded history and have remained common in artistic and spiritual designs [58]. Renowned examples include the Cretan labyrinth of Greek mythology [Fig. 6(c)], and the labyrinth decorating the floor of Chartres cathedral [Fig. 6(d)]. However, unlike ours, these and most other Labyrinth designs feature a dead end in the center. On the other hand, meanders [Fig. 6(e)] may close on themselves through the hole of the torus. In pattern-forming systems, unicursal labyrinths are rare. They were obtained under special conditions in simulations of a modified Swift-Hohenberg equation [62] and in experiments with ferrimagnetic garnet films in specific experimental protocols [63–65] [Fig. 6(f)]. In our case, they result from an emerging

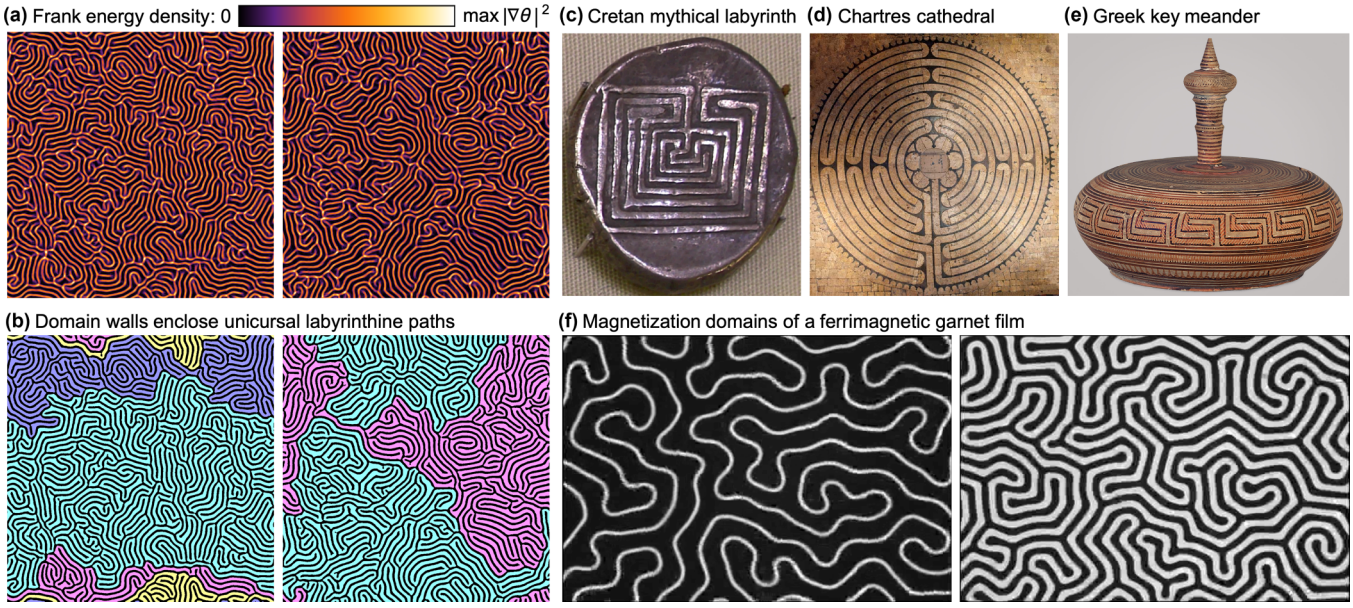

FIG. 6. Unicursal labyrinths. (a) Two examples of arrested treelike patterns formed by domain walls, with $Sv = -0.9$ (left) and $Sv = -1.1$ (right). (b) Processed negatives of panel (a) showing how domain walls (black) enclose a small and even number of unicursal labyrinths (four connected regions on the left and two on the right) that span the entire system (Appendix E, Fig. 14). The walls separating different labyrinths are self-connected across the periodic boundaries, unlike all other branches which feature endpoints. (c) The mythical labyrinth of Crete, shown on a silver coin from around 400 BC (by AlMare, reproduced from Wikimedia Commons [59], creative commons license [60]). (d) The labyrinth in the Chartres cathedral (courtesy of Père Emmanuel Blondeau and the secretariat de la Cathédrale Notre-Dame de Chartres). (e) Meander pattern known as the Greek key encircling a box (pyxis) from around 850 BC (reproduced from the Ref. [61]). (f) Out-of-plain magnetization domains of a ferrimagnetic garnet film, with black and white regions indicating opposite magnetizations. The amplitude of an external magnetic field favoring the black domain is gradually reduced from left to right, resulting in growth by folding of the white unicursal domain. Frames are desaturated snapshots from a video courtesy of Pietro Tierno.

topology of domain wall networks and they occur spontaneously and generically in the arrested regime.

V. UNCONSTRAINED Q-TENSOR MODEL

To place our results in a broader context, we now turn to the unconstrained active Q-tensor model, based on the Landau-de Gennes framework, which allows for the nucleation of true $\pm 1/2$ defect pairs. This enables us to (1) delineate the regime in which our defect-free findings remain applicable, and (2) explore the transition to the more familiar defect-laden behavior that arises when those conditions are no longer met. As in many previous studies, e.g., Refs. [34,66–71], we use the governing equations based on the Beris-Edwards model [72] for dimension $d = 2$ and $\mathrm{Re} = 0$ with the addition of the active nematic stress. These equations, expressed in our notation, together with details of the numerical scheme used to evolve $\mathbf{Q}$, are provided in Appendix D. For our discussion here, we define the nematic tensor in terms of the scalar order parameter s, quantifying local nematic alignment, and a unit director $\boldsymbol{n}$, as

$$Q_{\alpha\beta} = s\big(n_\alpha n_\beta - \tfrac{1}{2}\delta_{\alpha\beta}\big).$$

With respect to our constrained director-based formulation presented earlier, the key difference lies in the system's free energy:

$$F = \int (\mathcal{F}_\mathrm{e} + \mathcal{F}_\mathrm{b})\mathrm{d}^2\boldsymbol{r}, \tag{9}$$

where the elastic and bulk free energy densities are

$$\mathcal{F}_\mathrm{e} = \frac{K}{4}(\partial_\gamma Q_{\alpha\beta})(\partial_\gamma Q_{\alpha\beta}),$$

$$\mathcal{F}_\mathrm{b} = \frac{K}{4}\frac{1}{\epsilon^2}\big(-s_0^2 Q_{\alpha\beta}Q_{\alpha\beta} + (Q_{\alpha\beta}Q_{\alpha\beta})^2\big)$$

$$= \frac{K}{16}\frac{1}{\epsilon^2}s^2\big(-2s_0^2 + s^2\big).$$

We note that the one-constant elastic free energy density $\mathcal{F}_\mathrm{e}$ extends the Frank energy considered in Eq. (3). Now, rather than enforcing perfect nematic alignment, the bulk free energy density $\mathcal{F}_\mathrm{b}$ depends explicitly on the scalar order parameter s, which is allowed to vary in space and time. For convenience, we parametrize $\mathcal{F}_\mathrm{b}$ in terms of K, the defect core size ϵ, and the equilibrium scalar order s_0. Deep in the nematic phase, one has $s_0 \simeq 1$, favoring an equilibrium state with $s \simeq 1$. We thus fixed $s_0 = 1$ in our simulations, but allow to ϵ vary as it depends on the constituents of the system.

Because the width of domain walls scales as ℓ_a (the active length scale), the cost of elastic distortions per unit area at the walls scales as K/ℓ_a^2. On the other hand, the depth of the bulk potential is controlled by the factor K/ϵ^2 [see Fig. 7(a)]. Hence, a key control parameter that arises is the ratio $\epsilon^2/\ell_\mathrm{a}^2$. While the activity number $A = L^2/\ell_\mathrm{a}^2$ measures the strength of active forcing relative to system size, it is the ratio $\epsilon^2/\ell_\mathrm{a}^2$ that governs whether domain walls remain stable or give way to defect unbinding. We note that the regime $\epsilon \gtrsim \ell_\mathrm{a}$ leads to very different behavior beyond the scope of this work.

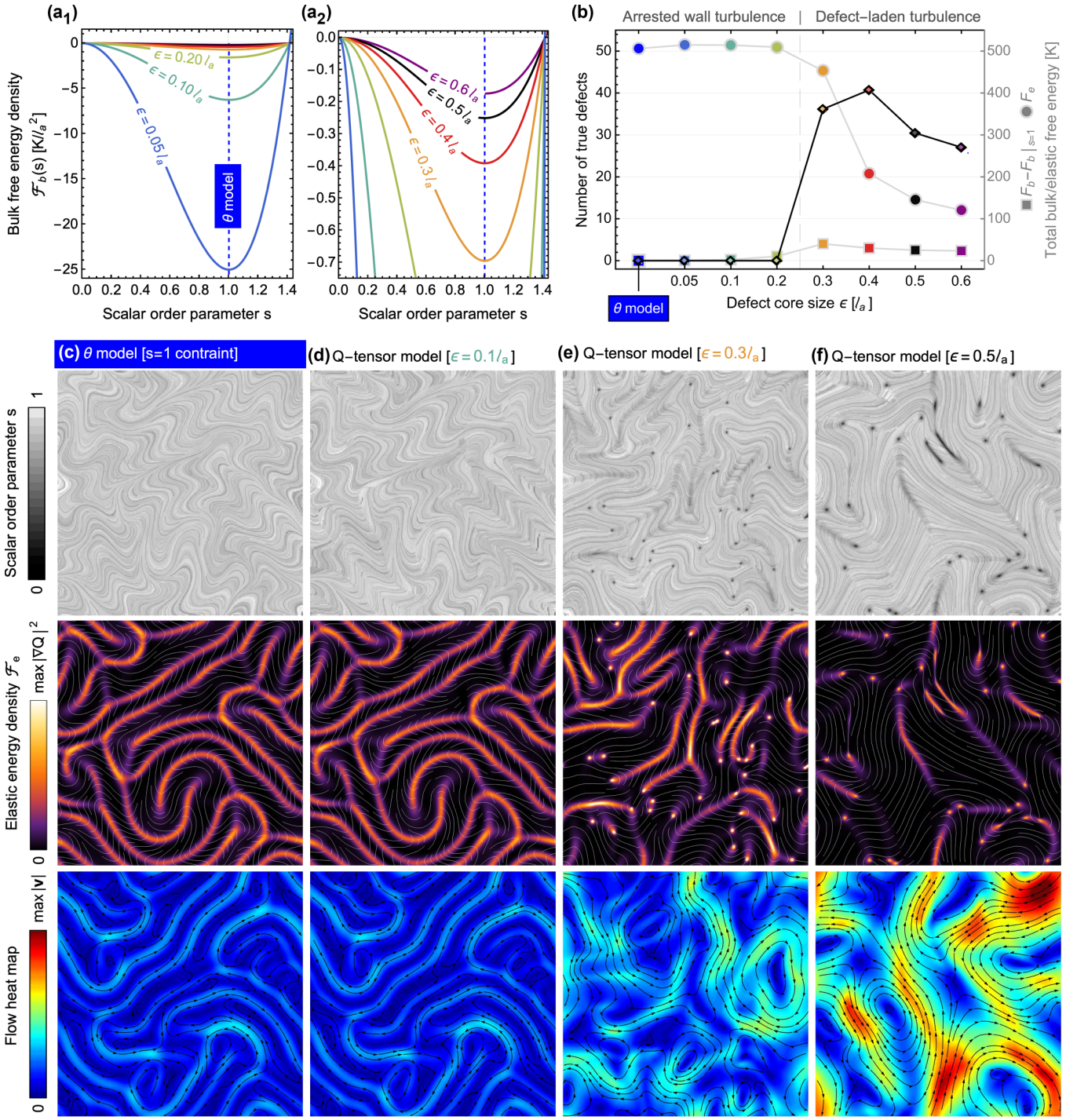

FIG. 7. Persistence of dynamical arrest and the transition to defect-laden turbulence. (a) Plots of the bulk free energy as a function of the scalar order parameter s for the values of ϵ explored in our simulations. Dashed blue line represents the θ model, for which $s = 1$ is enforced. The energy is shown in units of K/ℓ_a^2, characterizing elastic distortions. Note the difference in magnitude between panel (a_1), highlighting cases for which defects do not form, and panel (a_2), for which they do. (b) Statistical means of the total defect number (diamond markers, black line), the total bulk free energy (square markers, gray line), and total elastic free energy (circle markers, gray line), as a function of ϵ. These temporal averages characterize the fully developed turbulent state in our simulations (discarding initial transients). For timeseries and more detailed statistical breakdown, see Fig. 12. Typical snapshots from simulations of the θ model [panel (c)] and the full Q-tensor model, at increasing values of ϵ [panels (d)–(f)]. Top panels show the line integral convolution (LIC) representation of the director field $\boldsymbol{n}$, overlaid with a density plot of the scalar order parameter s, such that $s = 0$ is black and $s = 1$ is transparent (revealing the gray-scale LIC texture). True topological defects are seen as black spots and $s/2$, $\boldsymbol{n}$ are computed as the principal eigenpair of $\mathbf{Q}$. Panels of the center row show the elastic energy density along with white traces of $\boldsymbol{n}$. Bottom panels show the flow heatmap with black streamlines. In all simulations depicted here, we fixed $R = 1$, $S = 1$, $A = 10\,000$, $\nu = -1$ (the extensile rod-aligning regime), and set the same initial condition: a quiescent nematic state ($s = 1$) with a small angular perturbation. See also Movies S6 and S7 of the Supplemental Material [35].

To quantitatively compare Q-tensor simulations with the constrained case, we rederived the θ model directly from the Q-tensor framework under the constraint $s^2 = 1$ (Appendix D 5). The resulting equations are identical to those derived from the director-based formulation under $\boldsymbol{n}^2 = 1$, except that the Lagrange multiplier enforcing the constraint is independent of the flow field—a consequence of the orthogonality of flow alignment in the standard Q-tensor model. We found that this difference does not alter any of the qualitative defect-free behaviors reported thus far.

A. Arrested turbulence at finite defect core size

In the regime $\epsilon/\ell_a \ll 1$, defect cores are narrow compared to the active forcing scale, so defects (wherein $s \to 0$) carry a relatively high free energy cost [Fig. 7(a_1)]. As a result, domain walls persist without provoking the nucleation of defects [Fig. 7(b)], and the nematic forms arrested wall networks—just as in our constrained θ model [Figs. 7(c) and 7(d) and Movie S6 of the Supplemental Material [35]]. The persistence of this behavior at finite ϵ supports the view that dynamical arrest is a generic feature of active nematics, rather than a behavior limited to the constrained model. Beyond qualitative agreement, we find expected quantitative convergence to the θ model as $\epsilon \to 0$ (Appendix D 7, Fig. 11, and Movie S6 of the Supplemental Material [35]). Note that Q-tensor simulations become increasingly stiff and computationally expensive in this limit, making the θ model a more efficient and practical alternative.

B. Transition to defect-laden dynamics

When the ratio ϵ/ℓ_a exceeds a critical threshold (approximately 0.25 for fixed $S\nu = -1$), the potential well favoring nematic alignment becomes shallow compared to the elastic energy cost of orientational distortions, whose peak scales as K/ℓ_a^2 [Fig. 7(a_2)]. As a result, $\pm 1/2$ defects begin to nucleate [Fig. 7(b)], disrupting the formation of gridlocked wall patterns and giving rise to a more disordered, vortex-dominated turbulent state [Figs. 7(e) and 7(f) and Movie S7 of the Supplemental Material [35]]. In the transitional regime, we find that a modest increase in bulk free energy due to defect cores enables a dramatic reduction in the stored elastic free energy [Figs. 7(b) and 12]. This effect arises because defects, despite their intrinsic energetic cost, efficiently dissolve the high-energy walls that make up the network. As a consequence of the walls being less robust, the system no longer exhibits slow relaxation dynamics: Figure 12(a_1) shows that the number of true defects quickly reaches a statistically stationary state (albeit with strong fluctuations), in contrast to the slow relaxation of pseudodefects in the defect-free case [Fig. 5(c)].

VI. UNRAVELING ARREST: INTERPLAY OF DOMAIN WALL NETWORKS AND TRUE DEFECTS

The branched domain-wall networks that emerge in the extensile, rod-aligning regime (with defects suppressed) exhibit pronounced local peaks of elastic free energy. These distortion hot spots consistently arise near branchpoint pseudodefects, particularly along the incoming wall that splits into two outgoing branches [see, e.g., the final panels of Fig. 2(c)]. Viewing defect unbinding as a mechanism for efficiently lowering the system's free energy, we hypothesized that these hot spots would be predisposed to serve as defect nucleation sites upon quenching the defect core size.

The simulation shown in Movie S8 of the Supplemental Material [35] supports this hypothesis. Beginning from an arrested wall network generated at low ϵ/ℓ_a (specifically, $\epsilon = 0.2\,\ell_a$), we quenched the defect core size to above the critical threshold ($\epsilon = 0.35\,\ell_a$). Subsequent defect unbinding events were consistently initiated near branchpoint pseudodefects—though not all at once. Some branchpoints remain intact for some time, but these too are ultimately dissolved. Once unbound, the $+1/2$ defects are seen to travel along the bend walls on which they formed, effectively "unzipping" them as they move, as observed in previous computational studies [43–45]. Upon reaching an end-point pseudodefect (at the terminus of a branch), the motility of $+1/2$ defects can appear somewhat suppressed by the surrounding network geometry. Eventually, each $+1/2$ defect annihilates with a nearby $-1/2$ defect, creating aligned regions into which existing walls can expand or new walls can form. Near the critical threshold of ϵ/ℓ_a, this interchange continues in a highly dynamic fashion. Wall segments and pseudodefects coexist with a fluctuating population of unbound topological defects, resulting in a hybrid state that combines features of wall networks and defect-mediated turbulence (Movies S7 and S8 of the Supplemental Material [35]).

VII. DISCUSSION

In this work, we showed that flow alignment—the tendency of liquid crystals to reorient under shear—dramatically influences the spatiotemporal structure of defect-free active nematic turbulence (Fig. 1). For contractile flow-aligning active nematics, the chaos is characterized by fragmented nematic patterns, reduced total Frank free energy, and strong self-similar flows across a broad range of scales. We associate this strong large-scale turbulence to the underlying metastability of uniform and wall-laden states [38]. On the other hand, despite their chaotic dynamics, we find that extensile aligning active nematics self-organize into an arrested treelike pattern of nematic domain walls, with the flow strongly channeled along them [Figs. 1(d) and 1(e)]. This finding reveals a mechanism of pattern formation mediated by active turbulence, complementing those found in other studies [73–75]. In particular, our patterns enclose unicursal labyrinths (Fig. 6), which do not appear spontaneously in other pattern-forming systems.

The labyrinths in Fig. 6(b) span the entire system, but how far can they possibly extend? Further increasing the system size widens the range of chaotic self-similar flows, identified by the q^{-1} scaling of the velocity power spectrum [Fig. 1(g), blue]. These flows become stronger at larger scales, and hence they could potentially disrupt the arrested wall pattern for sufficiently large systems. At the scale where chaotic large-scale flows become as strong as the wall streams, which sustain the domain walls, the treelike network could lose its connectivity and fluctuate more strongly.

To test this idea, we performed defect-free simulations at even larger system sizes (Figs. S3 and S4 and Movies S9

and S10 of the Supplemental Material [35]). Since these simulations required substantially greater computational effort, we used the numerically advantageous θ model derived from the Q-tensor formulation (Appendix D 5). In the extensile, rod-aligning regime ($S\nu = -1.1$), we reached a system size at which the magnitude of chaotic, system-scale flows equaled that of the flows associated with the peak at the characteristic q (Fig. S3 of the Supplemental Material [35]). As anticipated, a widespread wall network develops with a selected wavelength (Fig. S4 of the Supplemental Material [35]), but frequent fracturing events prevent it from persistently spanning the entire system (Movie S9 of the Supplemental Material [35]). In contrast, in the contractile aligning case ($S\nu = +1.1$), dynamical arrest was not at play to begin with, so increasing the system size did not lead to qualitative changes (Movie S10 of the Supplemental Material [35]).

The arrested state does not show long-range correlations in the nematic order parameter (Fig. 9, blue). This is reminiscent of some passive systems, such as spin ice, that feature frustration in the absence of long-range geometrical correlations [76]. Similarly, our pattern features short-range disorder and is yet connected over long distances. Therefore, we propose that the unicursal labyrinths exhibit a form of long-range topological order stemming from emergent connectivity rules associated with the folding, branching, extension, and self-avoidance of the domain walls.

In the fully developed turbulent state, both the arrested and nonarrested regimes manifest a selected wavelength. This wavelength is significantly greater than the active length ℓ_a [Fig. 1(f)], and it also exceeds the critical wavelength of the spontaneous-flow instability. The wavelength selection mechanism is inherently nonlinear and two-dimensional; it is based on a balance between the coarsening of local striped patterns, which tends to enlarge the characteristic wavelength [Fig. 2(a)], and the bending and folding of walls that tends to reduce it [Fig. 2(b)]. A deeper understanding of the selection mechanism and its dependence on parameters remains an open question.

Whereas defect-free flows highlight surprising phenomena, most experiments and simulations in active nematics have been conducted in defect-laden regimes. Yet, the physics of the two regimes may intersect—as shown in our Q-tensor simulations [Fig. 7(e) and Movie S7 of the Supplemental Material [35]]. This crossover somewhat resembles the one found in polar fluids [77,78]. Actual nematic defects tend to nucleate along nematic domain walls, thereby dissolving them [44–46,79] (Movies S7 and S8 of the Supplemental Material [35]). This can be theoretically traced to the explicit form of the molecular field, $\mathbf{H} = -\delta F/\delta \mathbf{Q} + \frac{1}{2}\mathrm{tr}[\delta F/\delta \mathbf{Q}]\mathbf{I}$. As shown in Appendix D 3 (Remark D1), $\mathbf{H}$ has a component orthogonal to $\mathbf{Q}$, which drives rotations, and a component parallel to $\mathbf{Q}$ that drives variations in the scalar order parameter s. The latter is given by

$$\mathbf{H}_{\parallel} = \frac{K}{2}\left(\frac{1}{\epsilon^2}(1-s^2) + \frac{\nabla^2 s}{s} - 4(\nabla\theta)^2\right)\mathbf{Q},$$

where $\mathbf{Q} := s(\boldsymbol{nn} - \frac{1}{2}\mathbf{I})$ and $\boldsymbol{n} := (\cos\theta,\ \sin\theta)$. The first term in parentheses, stemming from the bulk free energy, restores s toward unity (the nematic phase). The second term, from the elastic energy, relaxes gradients in s, giving defects a finite core size. Crucially, the last term, also elastic, tends to *reduce* s in regions of strong orientational gradients (e.g., sharp domain walls)—highlighting a clear link between elastic distortions and the potential production of defects.

Additionally, an aspect not considered in our current modeling is that nematic constituents such as microtubules are observed to be depleted at defects [Fig. 4(g)], which likely lowers their energy cost and favors their nucleation [80]. The frequent dissolution of domain walls by defects explains why, in the instances where our wall network motifs can be seen in experiments [Figs. 4(f)–4(g)], they only have a short lifetime. We therefore argue that, in addition to their well-known role as *drivers* of turbulence by generating vorticity [32], defects also play an important role as *enablers* of stronger turbulent flows by breaking the potential gridlock, i.e., preventing dynamical arrest (Fig. 7 and Movies S7 and S8 of the Supplemental Material [35]).

Validating our predictions for defect-free active nematics presents an experimental challenge. By examining existing experimental images, we have already observed some of the phenomena, including the emergence of the three distinct pseudodefects and the formation of large labyrinthlike patterns by domain walls [54]. However, dynamical arrest—our primary prediction—has not yet been realized. This would require searching for active materials for which the nucleation of defect pairs were significantly more costly than in the experimental realizations studied thus far. As demonstrated in our Q-tensor simulations, defect-free active turbulence should be achievable for sufficiently large system sizes L, ensuring large dimensionless activity $A = (L/\ell_a)^2 \gg 1$, while keeping the defect-core size ϵ small enough ($\ell_a \gg \epsilon$) to preclude defect nucleation.

VIII. CONCLUSION

Our study of active nematic turbulence highlights the crucial role of topology beyond the existence of topological defects. We argue that the connectivity of domain walls, the existence of pseudodefects, and their interactions are key to understanding the dynamics of active nematics, from strong large-scale turbulence to dynamical arrest. Furthermore, in the presence of true topological defects, their interplay with pseudodefects adds another intriguing layer of complexity, as our Q-tensor simulations illustrate. Our results open avenues for experimental analysis and design, particularly in tracing the intricate web of domain walls, their orientation, and their nodes. They also raise a series of challenging theoretical questions, such as understanding the properties of pseudodefects, the nonlinear wavelength selection mechanism, and the nature of the long-range topological order of arrested states.

ACKNOWLEDGMENTS

Funding from the Spanish Ministry for Science and Innovation MICCINN/FEDER (PID2022-137713NB-C22 to I.L. and J.C.) and the Generalitat de Catalunya (AGAUR SGR-2021-00450 to I.L. and J.C. and ICREA Academia award to J.C.) is acknowledged. I.L. acknowledges support from the Flatiron Institute, part of the Simons Foundation. R.A. thanks the Isaac Newton Institute for Mathematical Sciences for

support and hospitality during the Programme *New Statistical Physics in Living Matter*, supported by EPSRC Grant No. EP/R014604/1, when work on this paper was undertaken.

DATA AVAILABILITY

The data that support the findings of this article are available from the authors upon reasonable request.

APPENDIX A: NUMERICAL SCHEME

Here, we describe our method for numerically integrating Eqs. (6)–(8). In what follows, the index n is the time iteration, dt is the time step, and $h = N^{-1}$ is the vertex spacing on our $N \times N$ square grid.

1. Solving momentum balance (pseudospectral method)

In each time iteration, we first solve for the streamfunction based on θ^n, the array representing the current director angle on the vertices. After rearranging terms and substituting $\hat{q}_{\alpha\beta}(\theta)$ and $\bar{q}_{\alpha\beta}(\theta)$ in Eq. (6), one has

$$\begin{aligned}\nabla^4\psi^n + G(\theta^n, \psi^n) &= S(d_1 \sin 2\theta^n + d_2 \cos 2\theta^n) \\ &\quad - \frac{R}{A}\Big(\frac{1}{2}\nabla^4\theta^n + (\partial_x\nabla^2\theta^n)\partial_y\theta^n - (\partial_y\nabla^2\theta^n)\partial_x\theta^n \\ &\quad + \nu(d_1 \cos 2\theta^n \nabla^2\theta^n - d_2 \sin 2\theta^n \nabla^2\theta^n)\Big), \qquad \text{(A1)}\end{aligned}$$

where we defined $d_1 := \frac{1}{2}(\partial_y^2 - \partial_x^2)$, $d_2 := \partial_y\partial_x$, and

$$G(\theta, \psi) := R\nu(d_1 \sin 2\theta h_\parallel(\theta, \psi) + d_2 \cos 2\theta h_\parallel(\theta, \psi)),$$

with

$$h_\parallel(\theta, \psi) = \nu(\sin 2\theta d_1\psi + \cos 2\theta d_2\psi).$$

To find the solution ψ^n, we employ a pseudospectral method, with all derivatives calculated in the space of the two-dimensional discrete Fourier transform (DFT) and all nonlinear operations performed in real space. Before each real-space multiplication, we apply the 2/3 dealiasing rule, truncating the Fourier modes with $|q_x|$ or $|q_y|$ greater than $\frac{2}{3}\pi N$.

We begin by computing the RHS of Eq. (A1), which is independent of ψ^n. Next, we note that $G(\theta^n, \psi^n)$, the second term on the LHS of Eq. (A1), consists of nonconstant coefficients combined with high-order derivatives. This defines a dense matrix in Fourier space that also varies in time. The high computation cost associated with building and inverting such a matrix at every time step renders direct inversion impractical. We therefore treat this term explicitly in a fixed-point iteration scheme, where we aim to compute a converging sequence $\{\psi^{n_k}\}_k$ (with $k = 0, 1, 2, \ldots$). Given an explicit approximation ψ^{n_k}, $G(\theta^n, \psi^{n_k})$ is computed pseudospectrally and transferred to the RHS. The subsequent iteration is then obtained by keeping the biharmonic term on the LHS implicit. By inverting the modified problem in Fourier space, the kth iteration is given by

$$\mathcal{F}[\psi^{n_{k+1}}] = \frac{1}{q^4}(\mathcal{F}[\mathrm{RHS}(\theta^n)] - \mathcal{F}[G(\theta^n, \psi^{n_k})]), \quad \forall q \neq 0, \qquad \text{(A2)}$$

where $\mathcal{F}[\cdot]$ indicates the DFT and $q = \|\boldsymbol{q}\|$. The mode $\boldsymbol{q} = 0$ in the streamfunction is always truncated as it has no bearing on the flow. To aid convergence, we initiate the sequence with the solution obtained in the previous time step, i.e., $\psi^{n_0} = \psi^{n-1}$. Iterations on k are performed until a convergence criterion for the residual error η is met. Formally, we compute

$$\eta_{k+1} = \frac{\int_\Omega (\psi^{n_{k+1}} - \psi^{n_k})^2}{\int_\Omega (\psi^{n_k})^2},$$

and we check whether $\eta_{k+1} < \epsilon$, with ϵ a small computational tolerance (typically 10^{-8}). While convergence is empirically tested, it is not guaranteed in the fixed-point method. With our chosen physical and numerical parameters, we find robust convergence so long as $|\nu| \lesssim 1.5$.

2. Computing the flow, vorticity, and flow-alignment rotations

After obtaining a convergent streamfunction ψ^n and before attending to Eq. (8), we compute the following fields pseudospectrally:

$$\begin{aligned}&v_x^n = \partial_y\psi^n, \quad v_y^n = -\partial_x\psi^n, \quad \omega^n = -\nabla^2\psi^n, \\ &C^n = -\hat{q}_{\alpha\beta}(\theta^n)\partial_\alpha\partial_\beta\psi^n = \cos 2\theta^n d_1\psi^n - \sin 2\theta^n d_2\psi^n. \qquad \text{(A3)}\end{aligned}$$

Respectively, these represent arrays of the flow components, vorticity, and a term proportional to flow-alignment rotations (C^n), defined on the vertices of the $N \times N$ grid.

3. Evolving the angle field (finite-element method)

We chose to evolve Eq. (8) with the finite-element method (FEM), using the open source package FreeFem++ [81]. The nodes of our triangular mesh $\mathcal{T}_h$, spanning the square domain Ω, coincide with the regular grid points. With this arrangement, it is straightforward to map the data v_α^n, ω^n, and C^n [Eq. (A3)] to the amplitudes of linear finite-element "hat functions."

To ensure stability of the scheme, we first tackle the convective term in Eq. (8) independently via the characteristics-Galerkin method [82]. Specifically, we solve the hyperbolic problem $\partial_t\theta + \boldsymbol{v}\cdot\nabla\theta = 0$ with the built-in **convect** function [81]: $\theta_{\mathrm{adv}}^n = \mathrm{convect}(\boldsymbol{v}^n, -dt, \theta^n)$.

Next, we formulate the time-discretized version of the rotations prescribed by Eq. (8),

$$(\theta^{n+1} - \theta_{\mathrm{adv}}^n)/dt - \frac{1}{2}\omega^n = \frac{1}{A}\nabla^2\theta^{n+1} - \nu C^n, \qquad \text{(A4)}$$

where we opted to handle the Laplacian term implicitly for enhanced stability.

To proceed with FEM, we write the weak form of Eq. (A4),

$$\begin{aligned}&\int_\Omega \theta^{n+1}\phi\, \mathrm{d}^2\boldsymbol{r} + \frac{dt}{A}\int_\Omega \nabla\theta^{n+1}\cdot\nabla\phi\, \mathrm{d}^2\boldsymbol{r} \\ &\quad = \int_\Omega \theta_{\mathrm{adv}}^n\phi\, \mathrm{d}^2\boldsymbol{r} + \frac{dt}{2}\int_\Omega \omega^n\phi\, \mathrm{d}^2\boldsymbol{r} - dt\,\nu\int_\Omega C^n\phi\, \mathrm{d}^2\boldsymbol{r}. \qquad \text{(A5)}\end{aligned}$$

The problem consists in finding a solution $\theta^{n+1} \in H^1(\Omega)$ for any arbitrary smooth test function $\phi : \Omega \to \mathbb{R}$.

The terms on the LHS of Eq. (A5) are bilinear (implicit) while those on the RHS are linear (explicit). In our code, θ and ϕ are represented by the basis functions spanning the continuous P2 finite-element space, i.e., polynomials of degree 2 defined piecewise on each element $K \in \mathcal{T}_h$. By imposing doubly periodic boundary conditions, the boundary term coming from integration by parts vanishes. The matrix defined by the LHS is inverted using the default **sparsesolver** in FreeFem++ [81].

4. Adding noise

To speed up the evolution towards fully developed active turbulence, we introduce small-amplitude stochastic fluctuations to $\partial_t\theta$ in the spirit of previous work [33]. We use a Gaussian white noise field $\xi(\boldsymbol{r},t)$ with zero mean and uncorrelated in both space and time, i.e., $\langle\xi(\boldsymbol{r},t)\rangle = 0$ and $\langle\xi(\boldsymbol{r},t)\xi(\boldsymbol{r}',t')\rangle = 2D\delta(\boldsymbol{r}-\boldsymbol{r}')\delta(t-t')$.

In more detail, we define ξ^n (the noise array at time $dt\,n$) in Fourier space by assigning to each mode a Gaussian random amplitude $a_{\boldsymbol{q}}$ and a random phase $\phi_{\boldsymbol{q}}$, expressed as $a_{\boldsymbol{q}}e^{i\phi_{\boldsymbol{q}}}$. The zero mode is truncated to impose a zero mean. To further counter aliasing, we also truncate the highest wave numbers for which $|q_x|$ or $|q_y|$ are greater than $\frac{2}{3}\pi N$. After taking the real part of the inverse DFT, the resulting noise is scaled by $\frac{\sqrt{3D}}{\sqrt{dth^2}}$. This factor ensures that the fluctuations are properly normalized, taking into account the space and time discretizations, as well as the 2/3 filtering. The normalized noise ξ^n is added to the RHS of Eq. (A4), resulting in an explicit integral term in the weak formulation [Eq. (A5)].

We verified that spatiotemporal chaos persists also in the absence of noise. Additionally, we found that increasing the noise amplitude enhances the velocity fluctuations, especially at large scales, thereby expanding the q^{-1} scaling region.

5. Additional notes

(1) The triangular FEM mesh $\mathcal{T}_h$ spans the entire periodic domain, resulting in $(N+1)\times(N+1)$ nodes. Thus, before proceeding to stage 3, we extend the real-space $N\times N$ arrays [Eq. (A3) and the noise ξ^n] so that the added data along the $x=1$ and $y=1$ edges matches the data along the $x=0$ and $y=0$ edges, respectively.

(2) To allow the pseudospectral computations involved in stage 1, the data stored in the P2 finite-element representation of θ^n are first downgraded to a P1 representation to obtain the field values on the $N\times N$ vertices.

Numerical parameters

In the large-scale simulations (Figs. 1 and 5, and Fig. S1, and Movies S1–S3, and S5 of the Supplemental Material [35]), we fixed $N=256$, $dt=0.01$, and $D=0.0025^2$. In the simulations depicted in Fig. 2 (Movie S4 of the Supplemental Material [35]), we fixed $N=128$, $dt=0.02$, and $D=0$ (zero noise).

6. Verification

We verified our computational solver for different parameter values. As demonstrated in Fig. 8, we compare the numerical output against two criteria: (1) long-time relaxation to predicted one-dimensional steady states (nonlinear striped patterns) that are stable at moderate activity levels [33,38] [Fig. 8(b)] and (2) the linear growth rate of small Fourier perturbations around the uniformly aligned quiescent state [33,38] [Fig. 8(c)].

APPENDIX B: SPECTRA

Here, we detail the computation of the spectra presented in Figs. 1(g)–1(i) and 9. In the equations below, we use the following notations:

(1) $\tilde{f}(\boldsymbol{q})$ is the two-dimensional DFT of $f(\boldsymbol{r})$, i.e., $\tilde{f} = \mathcal{F}[f]$.

(2) $\langle f(\boldsymbol{r})\rangle_{\boldsymbol{r}}$ is the spatial average of $f(\boldsymbol{r})$ over Ω.

(3) $\langle\tilde{f}(\boldsymbol{q})\rangle_\phi$ is the mean of all $\tilde{f}(\boldsymbol{q})$ for which $\boldsymbol{q} = q\,(\cos\phi, \sin\phi)$, i.e., an azimuthal average in Fourier space.

(4) $\langle\cdot\rangle$ is an ensemble average within fully developed active turbulence. In our long simulations, this is practically computed as the temporal mean for $t > t_T$, with t_T the onset time of a statistical steady state. To preclude initial transients, we empirically set $t_T = 200\tau_a$ (2×10^4 computational time iterations).

1. Velocity power spectrum

The velocity power spectrum in the 2D Fourier space is defined by [33]

$$E(\boldsymbol{q}) = \tfrac{1}{2}\langle\tilde{v}_\alpha^*(\boldsymbol{q})\tilde{v}_\alpha(\boldsymbol{q})\rangle = \tfrac{1}{2}q^2\langle|\tilde{\psi}(\boldsymbol{q})|^2\rangle. \tag{B1}$$

Under the assumption of statistical isotropy, one has

$$E(q) = 2\pi q\langle E(\boldsymbol{q})\rangle_\phi = \pi q^3\langle\langle|\tilde{\psi}(\boldsymbol{q})|^2\rangle\rangle_\phi. \tag{B2}$$

Since $\boldsymbol{v}$ is in units of $[L/\tau_a]$ and q is in units of $[L^{-1}]$, $E(q)$ is given in units of $[L/\tau_a^2]$ [Fig. 1(g)].

2. Frank energy spectrum

The Frank energy spectrum (or $\nabla\theta$ power spectrum) is defined by [33]

$$F_n(\boldsymbol{q}) = \frac{K}{2}\langle\mathcal{F}[\partial_\alpha\theta]^*(\boldsymbol{q})\mathcal{F}[\partial_\alpha\theta](\boldsymbol{q})\rangle = \frac{K}{2}q^2\langle|\tilde{\theta}(\boldsymbol{q})|^2\rangle. \tag{B3}$$

Under the assumption of statistical isotropy,

$$F_n(q) = 2\pi q\langle F_n(\boldsymbol{q})\rangle_\phi = \pi K q^3\langle\langle|\tilde{\theta}(\boldsymbol{q})|^2\rangle\rangle_\phi. \tag{B4}$$

Because q is in units of $[L^{-1}]$, $F_n(\boldsymbol{q})$ is given in units of $[K/L^3]$ [Fig. 1(h)].

3. Correlation time spectra

The nematic order parameter in our case, with the scalar amplitude fixed to 1, is the tensor $\hat{q}_{\alpha\beta} = n_\alpha n_\beta - 1/2\,\delta_{\alpha\beta}$ (not be confused with the wave vector $\boldsymbol{q}$). In terms of θ,

$$\hat{q} = \frac{1}{2}\begin{pmatrix}\cos 2\theta & \sin 2\theta\\ \sin 2\theta & -\cos 2\theta\end{pmatrix}. \tag{B5}$$

We define $\mathcal{C}_{\hat{q}\hat{q}}(\boldsymbol{x},\tau)$ as the space-time autocorrelation function of $\hat{q}$,

$$\mathcal{C}_{\hat{q}\hat{q}}(\boldsymbol{x},\tau) = \langle\langle\hat{q}_{\alpha\beta}(\boldsymbol{r},t)\hat{q}_{\alpha\beta}(\boldsymbol{r}+\boldsymbol{x},t+\tau)\rangle_{\boldsymbol{r}}\rangle, \tag{B6}$$

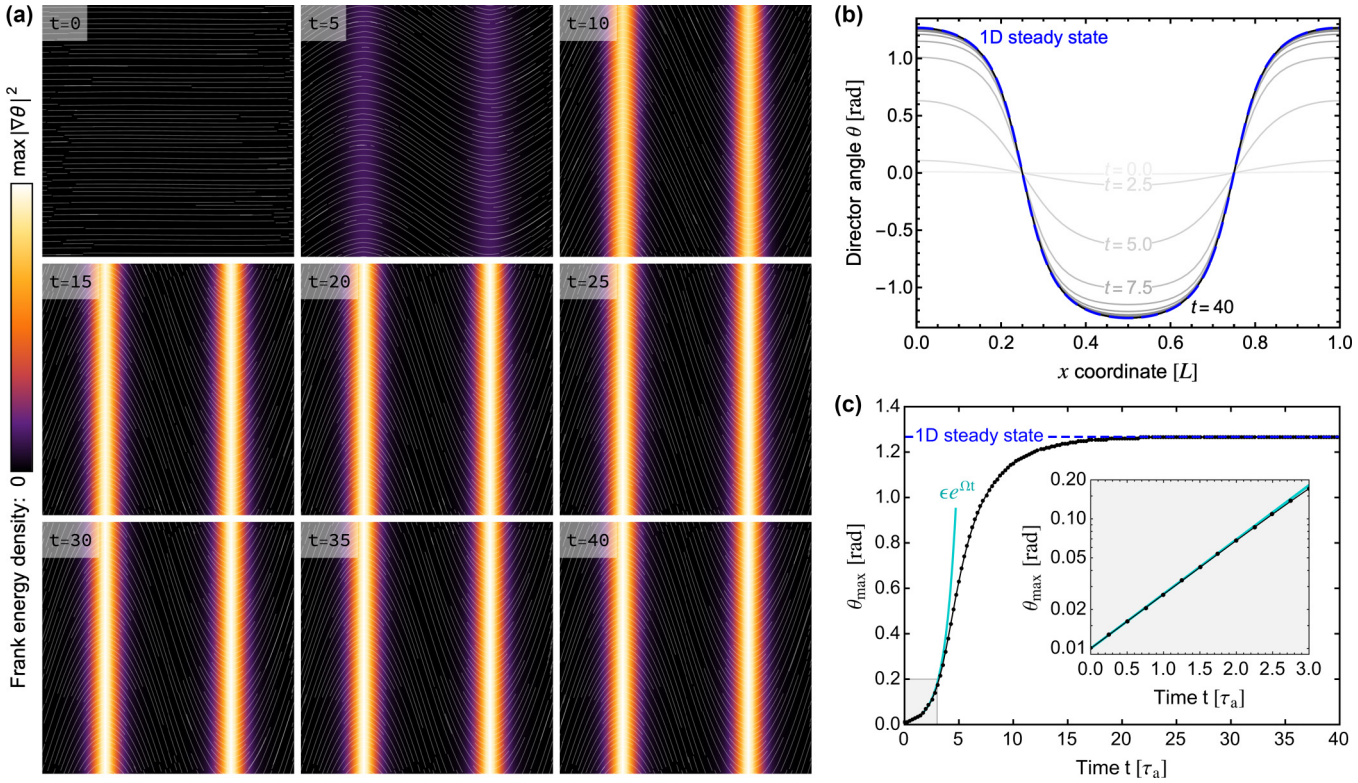

FIG. 8. Verification of the numerical scheme. (a) Consecutive snapshots from a simulation initiated with a small bending modulation about the uniformly aligned state: $\theta(\boldsymbol{r}, t=0) = \epsilon\cos(2\pi x)$, with $\epsilon = 0.01$. Parameter values were set to $R = 1$, $\nu = -1.1$, $A = 1000$, and $S = 1$ (extensile stress). Numerical parameters were set to $N = 64$, $dt = 0.01$, and $D = 0$ (zero noise). Color indicates the Frank energy, $|\nabla\theta|^2$, and white lines trace the director $\boldsymbol{n}$. (b) We plot the numerical data corresponding to a horizontal slice, $\theta(x, y = 0)$, for increasing times, starting from $t = 0$ (lightest gray) up to $t = 40\tau_a$ (black) in intervals of $2.5\tau_a$. It is shown that the angle profile relaxes on the predicted 1D steady state (dashed blue), obtained for the same parameter values as explained in our recent work [38]. (c) The maximum angle is plotted as a function of time in our simulation (black). First, it is shown that the modulation grows exponentially in time with the growth rate Ω matching the linear stability dispersion relation [38] (cyan). The gray inset is a log-scale plot comparing the simulation results with this explicit prediction for small perturbations. Additionally, it is demonstrated that the maximal angle in the simulation relaxes at long times to the value predicted by the 1D steady state [38] (dashed blue).

where $\boldsymbol{x}$ is the two point vector and τ is the lag time. For a given τ, the frames considered in the time average correspond to $t_T \leqslant t \leqslant T - \tau$, with T the total runtime of the simulation.

The spatial Fourier transform of $\mathcal{C}_{\hat{q}\hat{q}}$ is then

$$\begin{aligned}\tilde{\mathcal{C}}_{\hat{q}\hat{q}}(\boldsymbol{q},\tau) &= \langle \mathcal{F}[\hat{q}_{\alpha\beta}]^*(\boldsymbol{q},t)\mathcal{F}[\hat{q}_{\alpha\beta}](\boldsymbol{q},t+\tau)\rangle \\ &= \frac{1}{2}\langle \mathcal{F}[\cos 2\theta]^*(\boldsymbol{q},t)\mathcal{F}[\cos 2\theta](\boldsymbol{q},t+\tau)\rangle \\ &\quad + \frac{1}{2}\langle \mathcal{F}[\sin 2\theta]^*(\boldsymbol{q},t)\mathcal{F}[\sin 2\theta](\boldsymbol{q},t+\tau)\rangle. \quad \text{(B7)}\end{aligned}$$

For each mode $\boldsymbol{q}$, we fit the time series $\tilde{\mathcal{C}}_{\hat{q}\hat{q}}(\boldsymbol{q},\tau)$ to an exponential $\tilde{\mathcal{C}}_{\hat{q}\hat{q}}(\boldsymbol{q},0)e^{-\tau/\tau_{\hat{q}}}$, with $\tau_{\hat{q}}$ the fitting parameter, using the **NonlinearModelFit** function in Mathematica (TM). This fitting gives $\tau_{\hat{q}}(\boldsymbol{q})$. The azimuthal average $\tau_{\hat{q}}(q) = \langle\tau_{\hat{q}}(\boldsymbol{q})\rangle_\phi$ is shown in Fig. 1(i) (dark data points).

Next, we define the space-time autocorrelation function of the flow $\boldsymbol{v}$:

$$\mathcal{C}_{\boldsymbol{vv}}(\boldsymbol{x},\tau) = \langle\langle v_\alpha(\boldsymbol{r},\boldsymbol{t})v_\alpha(\boldsymbol{r}+\boldsymbol{x},t+\tau)\rangle_{\boldsymbol{r}}\rangle. \quad \text{(B8)}$$

The spatial Fourier transform of $\mathcal{C}_{\boldsymbol{vv}}$ is given by

$$\begin{aligned}\tilde{\mathcal{C}}_{\boldsymbol{vv}}(\boldsymbol{q},\tau) &= \langle\tilde{v}_\alpha^*(\boldsymbol{q},t)\tilde{v}_\alpha(\boldsymbol{q},t+\tau)\rangle \\ &= q^2\langle\tilde{\psi}^*(\boldsymbol{q},t)\tilde{\psi}(\boldsymbol{q},t+\tau)\rangle. \quad \text{(B9)}\end{aligned}$$

Note that $E(\boldsymbol{q}) = \frac{1}{2}\tilde{\mathcal{C}}_{\boldsymbol{vv}}(\boldsymbol{q},\tau=0)$ [see Eq. (B1)].

For each mode $\boldsymbol{q}$, we fit the time series $\tilde{\mathcal{C}}_{\boldsymbol{vv}}(\boldsymbol{q},\tau)$ to an exponential $\tilde{\mathcal{C}}_{\boldsymbol{vv}}(\boldsymbol{q},0)e^{-\tau/\tau_v}$, with τ_v the fitting parameter. This fitting gives $\tau_v(\boldsymbol{q})$. The azimuthal average $\tau_v(q) = \langle\tau_v(\boldsymbol{q})\rangle_\phi$ is shown in Fig. 1(i) (light data points).

4. Nematic tensor power spectrum

The nematic tensor power spectrum is defined by

$$W(\boldsymbol{q}) = \langle\mathcal{F}[\hat{q}_{\alpha\beta}]^*(\boldsymbol{q})\mathcal{F}[\hat{q}_{\alpha\beta}](\boldsymbol{q})\rangle. \quad \text{(B10)}$$

By this definition, one has $W(\boldsymbol{q}) = \tilde{\mathcal{C}}_{\hat{q}\hat{q}}(\boldsymbol{q},\tau=0)$ [see Eq. (B7)].

Under the assumption of statistical isotropy,

$$\begin{aligned}W(q) &= 2\pi q\langle W(\boldsymbol{q})\rangle_\phi \\ &= \pi q\big\langle\langle\mathcal{F}[\cos 2\theta]^*(\boldsymbol{q})\mathcal{F}[\cos 2\theta](\boldsymbol{q})\rangle \\ &\quad + \langle\mathcal{F}[\sin 2\theta]^*(\boldsymbol{q})\mathcal{F}[\sin 2\theta](\boldsymbol{q})\rangle\big\rangle_\phi. \quad \text{(B11)}\end{aligned}$$

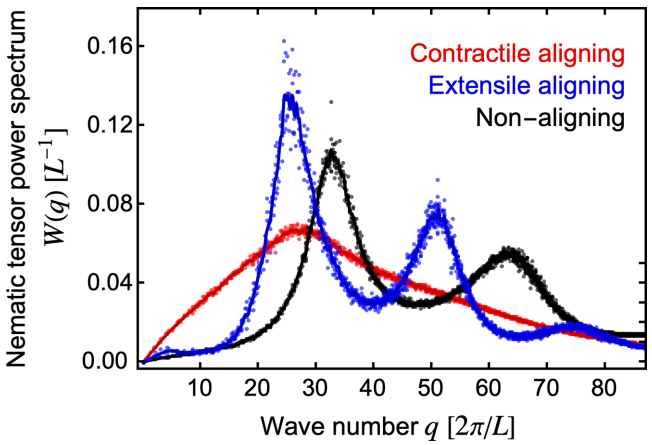

FIG. 9. Power spectrum of the order parameter in active nematic turbulence. Shown is the power spectrum of the nematic tensor, $\hat{q}_{\alpha\beta} = n_\alpha n_\beta - 1/2\,\delta_{\alpha\beta}$, in the contractile flow-aligning ($S\nu = +1.1$, red), extensile flow-aligning ($S\nu = -1.1$, blue), and nonaligning ($\nu = 0$, black) cases. For the definition of $W(q)$, see Eq. (B11). Lines represent a smoothed (Gaussian) interpolation of the computed data points. Parameter values are as in Fig. 1 and Fig. S1 of the Supplemental Material [35]. For arrested turbulence (blue), this spectrum features a narrow peak with its associated harmonics. For strong large-scale turbulence (red), such peaks are washed out. In all regimes, low-q correlations are essentially absent.

Since $\hat{q}$ is dimensionless and q is in units of $[L^{-1}]$, $W(\boldsymbol{q})$ is given in units $[L^{-1}]$ (Fig. 9).

APPENDIX C: TOPOLOGICAL PSEUDOCHARGE OF DOMAIN WALL NODES

In arrested and nearly arrested states, arising in the extensile aligning regime, the domain walls are organized in a treelike network. One can associate a planar, directed graph to this network, with three types of nodes: startpoints, endpoints, and branchpoints, as described in Figs. 3(a)–3(c). In the long-time asymptotics, the startpoints are only residual, and the ageing tree is mostly formed by endpoints and branchpoints (Fig. 5 and Movie S5 of the Supplemental Material [35]). While these nodes are not topological defects of the nematic field, one can assign to them a pseudocharge that is conserved and contains useful information of topological nature, as discussed in this section. We emphasize that this pseudo-topology is an effective emergent property of the dynamics, which holds only for the appropriate parameter regimes and time asymptotics. Therefore, pseudodefects are dynamically stabilized but are not topologically stable in the sense that they can be removed by a continuous perturbation of the nematic field.

To define the topological pseudocharge, we first consider the change of angle across a nematic wall. To this end, we look for steady-state solutions of the director field in 1D, that is, with translational invariance in the direction along the wall. In this case, the angle varies only along the transverse coordinate s. In the steady state, the director profile across the wall obeys the 1D stationary equation [38]

$$\ell_a^2 \partial_s^2 \theta = \frac{S(1+\nu\cos 2\theta)(\sin 2\theta - \sin 2\bar{\theta})}{4 + R + R\nu^2 + 2R\nu\cos 2\theta}, \qquad \text{(C1)}$$

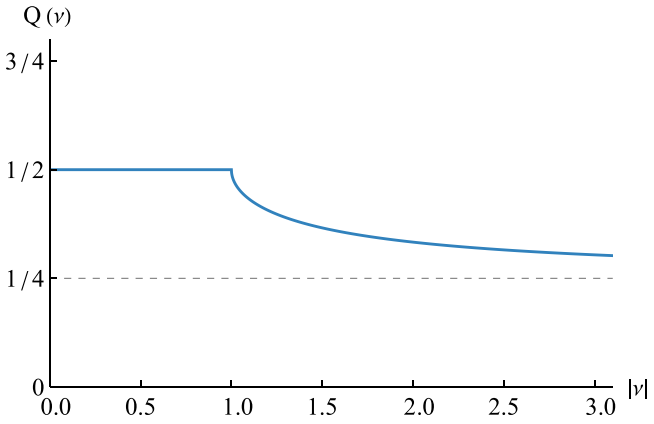

FIG. 10. Q as a function of $|\nu|$. Functional form of the elementary charge $Q(\nu)$. Positive pseudodefects have charge $+Q$, and negative ones $-Q$. For the tumbling regime $Q = 1/2$ and for the aligning regime Q decreases monotonically from 1/2 to 1/4.

where $\bar{\theta}$ is the orientation of the nematic director at the center of the domain wall. This equation supports sigmoidal angle profiles with an interface of thickness of the order of the active length ℓ_a that continuously connects two plateaux of uniform angle. As the interfaces separate regions of uniform angle, they are referred to as domain walls, also called kinks and antikinks in other contexts.

For $S\nu > -1$, the two plateaux values of the nematic angle are $\theta = \bar{\theta} \pm \frac{\pi}{2}$, so the total rotation of the nematic across the wall is $\Delta\theta = \pm\pi$. For $S\nu < -1$, the plateaux angles correspond to the so-called Leslie angle defined by $1 + \nu\cos 2\theta_L = 0$, which amounts to an angle rotation of $\Delta\theta = \pm(\pi - \arccos|\nu|^{-1})$ across the wall. We remark that the total angle variation across domain walls is independent of both the active length ℓ_a and the viscosity ratio R. For a domain wall centered at $s = s_i$, we define the smooth step functions $\Theta^{\pm}(s - s_i)$ that connect the plateau values via a total angle increment $\Delta\theta$, which is positive for Θ^+ and negative for Θ^-. The angle varies at a scale $\sim\ell_a$ about s_i. Similarly, the derivative with respect to the spatial coordinate s defines two peaked functions $\dot{\Theta}^{\pm}(s - s_i)$ such that, in the sharp-wall limit,

$$\lim_{\ell_a \to 0} \dot{\Theta}^{\pm}(s - s_i) = \Delta\theta\,\delta(s - s_i) \equiv \pm\frac{Q(\nu)}{2\pi}\delta(s - s_i). \qquad \text{(C2)}$$

Here, $Q(\nu)$ is the elementary pseudocharge function, defined as

$$Q(\nu) \equiv \frac{1}{2\pi}\int_{-\infty}^{+\infty} \dot{\Theta}_0^+ \mathrm{d}s > 0, \qquad \text{(C3)}$$

which gives, for $S\nu < 0$,

$$Q(\nu) = \frac{1}{2}\left(1 - \frac{1}{\pi}\mathcal{H}(|\nu| - 1)\arccos|\nu|^{-1}\right) > 0, \qquad \text{(C4)}$$

where $\mathcal{H}$ is the Heaviside step function. The elementary pseudocharge function $Q(\nu)$ takes the value 1/2 in the tumbling regime, and it spans the interval from 1/2 to 1/4 as $|\nu|$ is increased beyond 1. The functional form of $Q(\nu)$ is plotted in Fig. 10.

To define a topological pseudocharge of the pseudodefects, and of any closed domain in general, we recall that the total

angle variation along a closed loop must be

$$\oint \mathrm{d}\theta = \oint \dot{\theta}\, \mathrm{d}s = 0, \tag{C5}$$

with $\dot{\theta}\mathrm{d}s = \vec{\nabla}\theta \cdot \mathrm{d}\vec{s}$ where $\mathrm{d}\vec{s}$ describes the contour, with s the arclength coordinate. We are interested in the limit of small ℓ_a, or equivalently, to situations where the separation between consecutive walls is much larger than the wall thickness, so that there is no significant overlap between $\dot{\Theta}^{\pm}(s - s_i)$ and $\dot{\Theta}^{\pm}(s - s_j)$, i.e., $|s_i - s_j| \gg \ell_a$. Then, we can distinguish two scales of variation of the nematic orientation: The inner region of the domain wall where the nematic variation is fast ($\dot{\theta} \sim \ell_a^{-1}$), and the outer regions where it is slow ($\dot{\theta} \sim \ell_a^0$). Under these circumstances, we may define the pseudocharge as the part of the director rotation along a closed loop that takes place at the slow-variation (outer regions of the domain walls). In other words, we consider the total director rotation excluding the fast variation across the walls that are intersected by the loop.

Consider, for instance, an isolated endpoint pseudodefect [Fig. 3(c)], formed by a wall that points toward it, and consider a counterclockwise closed path Γ that contains it and intersects the center of the wall at $s = s_0$. We define the pseudocharge of this pseudodefect as

$$Q_\Gamma = \frac{1}{2\pi} \oint_\Gamma (\dot{\theta}(s) - \dot{\Theta}^-(s - s_0))\mathrm{d}s \tag{C6}$$

$$= \frac{1}{2\pi} \oint_\Gamma \dot{\Theta}^+(s - s_0)\, \mathrm{d}s > 0, \tag{C7}$$

which coincides strictly with $Q(\nu)$ in the sharp-wall limit. To subtract the localized fast variation of θ across the wall, we need to write $\Theta^-(s - s_0)$ because the nematic is rotating clockwise across the wall (decreasing angle), if the wall is oriented toward the interior of the path that encloses the endpoint. In general, the sense of rotation of the nematic across a wall is opposite (equal) to the sense of rotation of the closed loop when the wall points toward the interior (exterior) of the loop.

Similarly, for an isolated branchpoint we define the pseudocharge as the rotation of the director in regions excluding the walls along a closed loop enclosing the branchpoint [Fig. 3(b)]. In this case, we must subtract the fast variation across the three walls intersected by the integration path. Since there is always one wall pointing toward the interior and two pointing toward the exterior, the pseudocharge for a branchpoint, in the sharp-wall limit, will be $-Q(\nu)$.

For a general configuration with an arbitrary number of pseudodefects and associated walls, the total pseudocharge in the interior of a closed loop will be given by the sum of the pseudocharge of all the pseudodefects in it. We remark that it is not necessary to know the detailed structure of the nematic field in the interior, but only in the contour, as in the definition of the actual topological charge. In fact, the total pseudocharge in the interior of an arbitrary closed loop Γ is also given by

$$Q_\Gamma = (m_{\mathrm{in}} - m_{\mathrm{out}})Q(\nu), \tag{C8}$$

where m_{in} and m_{out} are the number of inward and outward domain walls crossed by the contour line, respectively.

In the case of domain walls with a small but finite thickness compared to typical wall separation, the elementary pseudocharge will slightly differ from the limiting value defined in Eq. (C3). In that case, consecutive walls partially overlap so that the angle profile does not reach the asymptotic value of the plateau, and the magnitude of the angle variation across the walls, $\Delta\theta$, is slightly smaller. This is the case in the wall patterns studied in this work, so in the main manuscript we refer to the values taken by the pseudotopological charge only as $\simeq Q(\nu)$. We remark, however, that the precise value of the elementary charge $Q(\nu)$ is not really informative of the relevant topological structure, that is, how walls are connected, but accounts for the detailed structure of the walls themselves. This may be important to determine their dynamical properties, such as their interactions or their rigidity to deformation. However, it is only the integer counts of positive and negative pseudodefects (or the counts of inward and outward wall intersections), i.e., the multiples of the elementary charge, that are informative of the overall qualitative structure inside a given domain.

In the sharp-wall limit $\ell_a \to 0$, the idea of a pseudodefect is reminiscent of Dirac's construction of magnetic monopoles, based on attaching to them the so-called Dirac string, which carries a quantized magnetic flux [49]. In that way, the magnetic monopole can be made consistent with Maxwell's equations. For instance, the total magnetic flux across a closed surface enclosing the magnetic monopole would be zero, as required by Gauss's theorem for the absence of net magnetic charge, because the flux generated by the monopole is canceled by that carried out by the string, which also crosses the surface. Similarly, in our problem, the wall attached to the pseudodefect provides a localized (fast) rotation of the director that cancels the (slow) rotation outside the wall to ensure the lack of true topological charge. In this way, the problem satisfies the local constraint of zero topological charge while mimicking with pseudodefects the director field around actual topological defects in a large region of space around them.

APPENDIX D: Q-TENSOR MODEL AND SIMULATIONS

We complement our analysis of defect-free active nematics with simulations of the full Q-tensor model to demonstrate the broader applicability of our findings. Specifically, we show that arrested domain-wall turbulence is not merely a feature of the constrained director-based model, but rather a robust phenomenon that arises when defect nucleation is energetically suppressed. In the generic model, the ratio of the defect core size ϵ to the active length ℓ_a emerges as a key control parameter. When $\epsilon \ll \ell_a$, the free energy cost of nucleating topological defects exceeds that of forming networks of domain walls threaded by pseudodefects. Hence, large-scale labyrinthine patterns consistently arise in the extensile, rod-aligning regime when $L \gg \ell_a \gg \epsilon$.

We further show that as the core size exceeds a critical threshold, defect nucleation destabilizes the domain walls, ultimately destroying the gridlocked network and leading to qualitatively different dynamics. Near this threshold, we find that $\pm 1/2$ defects preferentially unbind at distortion hot spots associated with the branchpoint pseudodefects. This finding highlights an interesting connection between the zigzagging

and branching of domain walls and the subsequent formation of topological disclinations.

1. Definition and energetics

The nematic order parameter in 2D is a symmetric, traceless tensor defined by

$$Q_{\alpha\beta} = s\big(n_\alpha n_\beta - \tfrac{1}{2}\delta_{\alpha\beta}\big),$$

where s is the scalar order parameter and $\boldsymbol{n}$ is a unit director. The tensor $\mathbf{Q}$ then has eigenvalues $\pm s/2$, with $\boldsymbol{n}$ the eigenvector associated with the positive eigenvalue.

We adopt the Landau-de Gennes free energy,

$$F = \int (\mathcal{F}_\mathrm{e} + \mathcal{F}_\mathrm{b})\mathrm{d}^2\boldsymbol{r}, \tag{D1}$$

where

$$\mathcal{F}_\mathrm{e} = \frac{K}{4}(\partial_\gamma Q_{\alpha\beta})(\partial_\gamma Q_{\alpha\beta}),$$
$$\mathcal{F}_\mathrm{b} = \frac{K}{4}\frac{1}{\epsilon^2}\big(-s_0^2 Q_{\alpha\beta}Q_{\alpha\beta} + (Q_{\alpha\beta}Q_{\alpha\beta})^2\big).$$

Here, we defined the elastic distortion energy $\mathcal{F}_\mathrm{e}$ using a single constant K. The prefactor $1/4$ ensures that, when $s = 1$, the expression reduces exactly to the one-constant Frank energy density of the director-based model: $\frac{K}{2}(\partial_\alpha n_\beta)(\partial_\alpha n_\beta)$, when $|\boldsymbol{n}| = 1$ [see Eq. (3)]. The bulk free energy $\mathcal{F}_\mathrm{b}$ includes quadratic and quartic thermotropic terms. The sign and ratio of the coefficients are chosen to correspond to a temperature below the isotropic-nematic transition. We parametrize these in terms of K and a characteristic length scale ϵ, known as the defect core size. The parameter s_0 sets the equilibrium value of the nematic scalar order. Hereafter, we fix $s_0 = 1$, corresponding to a system that would, at equilibrium, lie deep in the nematic phase.

The orientational field $\mathbf{H}$ is a symmetric traceless tensor given by

$$H_{\alpha\beta} = -\frac{\delta F}{\delta Q_{\alpha\beta}} + \frac{\delta_{\alpha\beta}}{2}\mathrm{tr}\frac{\delta F}{\delta Q_{\gamma\delta}}$$
$$= \frac{K}{2}(\nabla^2 Q_{\alpha\beta} + \epsilon^{-2}(1 - s^2)Q_{\alpha\beta}), \tag{D2}$$

where we substituted $s^2 = 2\,\mathrm{tr}\,\mathbf{Q}^2 = 2Q_{\gamma\delta}Q_{\gamma\delta}$, clarifying how the bulk term in $\mathbf{H}$ acts to restore the equilibrium scalar order. We emphasize that the key difference from our constrained director-based model is that nematic alignment (here encoded in s) is no longer enforced by a Lagrange multiplier, but may vary dynamically.

2. Hydrodynamics

As in Eq. (1), momentum balance reads

$$0 = -\partial_\alpha P + \partial_\beta\big(\sigma^\mathrm{a}_{\alpha\beta} + \sigma^\mathrm{E}_{\alpha\beta} + \sigma_{\alpha\beta}\big). \tag{D3}$$

In terms of $\mathbf{Q}$ and $\mathbf{H}$, and defining $\tilde{Q}_{\alpha\beta} \equiv Q_{\alpha\beta} + \delta_{\alpha\beta}/2$, the stress contributions are given by

$$\sigma^\mathrm{a}_{\alpha\beta} = Q_{\alpha\gamma}H_{\gamma\beta} - H_{\alpha\gamma}Q_{\gamma\beta}, \tag{D4}$$

$$\sigma^\mathrm{E}_{\alpha\beta} = -\frac{\delta F}{\delta(\partial_\alpha Q_{\gamma\delta})}\partial_\beta Q_{\gamma\delta} = -\frac{K}{2}(\partial_\alpha Q_{\gamma\delta})(\partial_\beta Q_{\gamma\delta}), \tag{D5}$$

$$\sigma_{\alpha\beta} = 2\eta v_{\alpha\beta} - \zeta Q_{\alpha\beta} + \nu(\tilde{Q}_{\alpha\gamma}H_{\gamma\beta} + H_{\alpha\gamma}\tilde{Q}_{\gamma\beta} - 2(Q_{\gamma\delta}H_{\gamma\delta})\tilde{Q}_{\alpha\beta}), \tag{D6}$$

where η is the shear viscosity, $v_{\alpha\beta} = (\partial_\alpha v_\beta + \partial_\beta v_\alpha)/2$, and ζ is the active stress parameter.

3. Nematodynamics

As in the passive theory (Beris-Edwards model [72]), the Q tensor evolves as

$$\partial_t Q_{\alpha\beta} + v_\gamma\partial_\gamma Q_{\alpha\beta} + \omega_{\alpha\gamma}Q_{\gamma\beta} - Q_{\alpha\gamma}\omega_{\gamma\beta} = \Gamma H_{\alpha\beta} - \nu(v_{\alpha\gamma}\tilde{Q}_{\gamma\beta} + \tilde{Q}_{\alpha\gamma}v_{\gamma\beta} - 2(Q_{\gamma\delta}\partial_\gamma v_\delta)\tilde{Q}_{\alpha\beta}), \tag{D7}$$

where $\omega_{\alpha\beta} = (\partial_\alpha v_\beta - \partial_\beta v_\alpha)/2$ and Γ scales the response of $\mathbf{Q}$ to the molecular field $\mathbf{H}$. When $s = 1$, we wish to recover the same expression as in the $|\boldsymbol{n}| = 1$ limit of the director-based model. To that end, we set $\Gamma = 2/\gamma$, with γ the rotational viscosity.

Remark D 1 (Orthogonal and parallel components of $\mathbf{H}$*).* By substituting

$$Q_{\alpha\gamma} = s\big(n_\alpha n_\beta - \tfrac{1}{2}\delta_{\alpha\beta}\big) = \frac{s}{2}\begin{pmatrix}\cos 2\theta & \sin 2\theta \\ \sin 2\theta & -\cos 2\theta\end{pmatrix}$$

in Eq. (D2), we find that the contribution to $\partial_t\mathbf{Q}$ arising from the molecular field is given by

$$\frac{2}{\gamma}\mathbf{H} = \frac{K}{\gamma}\left(\nabla^2\mathbf{Q} + \frac{1}{\epsilon^2}(1 - s^2)\mathbf{Q}\right)$$
$$= \frac{K}{\gamma}\left(\frac{4\nabla s\cdot\nabla\theta}{s} + 2\nabla^2\theta\right)\mathbf{Q}^\perp$$
$$+ \frac{K}{\gamma}\left(\frac{\nabla^2 s}{s} - 4(\nabla\theta)^2 + \frac{1}{\epsilon^2}(1 - s^2)\right)\mathbf{Q},$$

where

$$Q^\perp_{\alpha\beta} = Q_{\alpha\gamma}\epsilon_{\gamma\beta} = \frac{s}{2}\begin{pmatrix}-\sin 2\theta & \cos 2\theta \\ \cos 2\theta & \sin 2\theta\end{pmatrix}.$$

The terms proportional to $\mathbf{Q}^\perp$ drive rotations, while those along $\mathbf{Q}$ regulate the scalar order parameter s. In particular, the term $-4(\nabla\theta)^2\mathbf{Q}$ acts to reduce s, pushing the system away from perfect alignment. Assuming θ varies on the active length scale ℓ_a, this contribution scales as $-1/\ell_\mathrm{a}^2$. On the other hand, the term proportional to $1/\epsilon^2$ tends to restore s toward unity. This competition explains why the ratio ϵ/ℓ_a plays a central role in determining whether the system remains uniformly nematic or gives way to defect nucleation.

4. Dimensionless (Q_{11}, Q_{12})-ψ formulation

For consistency, we adopt the same nondimensionalization as in the director-based model: lengths are scaled by the system size L, time by the active timescale $\tau_\mathrm{a} = \eta/|\zeta|$, stress by the activity scale $|\zeta|$, and the orientational field by K/L^2. We then define the problem in terms of the sign of active stress $S = \pm 1$ (positive for extensile), the viscosity ratio $R = \gamma/\eta$, the activity number $A = RL^2|\zeta|/K = L^2/\ell_\mathrm{a}^2$, and the dimensionless defect core size $\varepsilon = \epsilon/L$. In the following,

we denote adimensionalized fields and derivatives with top bar [e.g, $\bar{\nabla} = L\nabla$, $\bar{\partial}_t = \tau_a \partial_t$, $\bar{v} = (\tau_a/L)v$].

We now define $\mathbf{Q}$ and the adimensional orientational field $\bar{\mathbf{H}}$ in terms of Q_{11} and Q_{12}, for which we seek a closed-form model:

$$\mathbf{Q} = \begin{pmatrix} Q_{11} & Q_{12} \\ Q_{12} & -Q_{11} \end{pmatrix}, \quad \bar{\mathbf{H}} = \begin{pmatrix} \bar{H}_{11} & \bar{H}_{12} \\ \bar{H}_{12} & -\bar{H}_{11} \end{pmatrix}, \tag{D8}$$

where

$$\bar{H}_{11} = \frac{L^2}{K} H_{11} = \frac{1}{2}(\bar{\nabla}^2 Q_{11} + \varepsilon^{-2}(1 - s^2)Q_{11}), \tag{D9}$$

$$\bar{H}_{12} = \frac{L^2}{K} H_{12} = \frac{1}{2}(\bar{\nabla}^2 Q_{12} + \varepsilon^{-2}(1 - s^2)Q_{12}), \tag{D10}$$

and

$$s^2 = 4\big(Q_{11}^2 + Q_{12}^2\big). \tag{D11}$$

The adimensional stress terms read

$$\bar{\sigma}^{\mathrm{a}}_{\alpha\beta} = \frac{\sigma^{\mathrm{a}}}{|\zeta|} = \frac{R}{A}(Q_{\alpha\gamma}\bar{H}_{\gamma\beta} - \bar{H}_{\alpha\gamma}Q_{\gamma\beta}), \tag{D12}$$

$$\bar{\sigma}^{\mathrm{E}}_{\alpha\beta} = \frac{\sigma^{\mathrm{E}}}{|\zeta|} = -\frac{R}{2A}(\bar{\partial}_\alpha Q_{\gamma\delta})(\bar{\partial}_\beta Q_{\gamma\delta}), \tag{D13}$$

$$\bar{\sigma}_{\alpha\beta} = \frac{\sigma}{|\zeta|} = 2\bar{v}_{\alpha\beta} - SQ_{\alpha\beta} + \frac{R\,v}{A}(\tilde{Q}_{\alpha\gamma}\bar{H}_{\gamma\beta} + \bar{H}_{\alpha\gamma}\tilde{Q}_{\gamma\beta} - 2(Q_{\gamma\delta}\bar{H}_{\gamma\delta})\tilde{Q}_{\alpha\beta}). \tag{D14}$$

The adimensional version of Eq. (D7) reads

$$\bar{\partial}_t Q_{\alpha\beta} + \bar{v}_\gamma \bar{\partial}_\gamma Q_{\alpha\beta} + \bar{\omega}_{\alpha\gamma}Q_{\gamma\beta} - Q_{\alpha\gamma}\bar{\omega}_{\gamma\beta} = \frac{2}{A}\bar{H}_{\alpha\beta} - v(\bar{v}_{\alpha\gamma}\tilde{Q}_{\gamma\beta} + \tilde{Q}_{\alpha\gamma}\bar{v}_{\gamma\beta} - 2(Q_{\gamma\delta}\bar{\partial}_\gamma \bar{v}_\delta)\tilde{Q}_{\alpha\beta}). \tag{D15}$$

Hereafter, we shall consider only dimensionless fields and derivatives and omit the overbar notation. Then, in terms of the stream function ψ, we obtain for Q_{11} and Q_{12},

$$\partial_t Q_{11} + (\partial_y\psi, -\partial_x\psi)\cdot\nabla Q_{11} - Q_{12}\nabla^2\psi = \frac{2}{A}H_{11} - v\big(\big(1 - 4Q_{11}^2\big)d_2\psi - 4Q_{11}Q_{12}d_1\psi\big), \tag{D16}$$

$$\partial_t Q_{12} + (\partial_y\psi, -\partial_x\psi)\cdot\nabla Q_{12} + Q_{11}\nabla^2\psi = \frac{2}{A}H_{12} - v\big(\big(1 - 4Q_{12}^2\big)d_1\psi - 4Q_{11}Q_{12}d_2\psi\big), \tag{D17}$$

where we reintroduced the notation $d_1 := \frac{1}{2}(\partial_y^2 - \partial_x^2)$, $d_2 := \partial_y\partial_x$.

To derive an equation for the stream function ψ, we evaluate the curl of Eq. (D3), which eliminates the pressure from the problem. The term coming from the antisymmetric stress, defined in Eq. (D12), reads

$$\begin{aligned}\mathrm{curl}(\nabla\cdot\sigma^{\mathrm{a}}) &= \epsilon_{\gamma\alpha}\partial_\gamma\big(\partial_\beta\sigma^{\mathrm{a}}_{\alpha\beta}\big) \\ &= \epsilon_{\gamma\alpha}\partial_\gamma\big(\partial_\beta\epsilon_{\alpha\beta}\sigma^{\mathrm{a}}_{12}\big) = -\delta_{\gamma\beta}\partial_\gamma\partial_\beta\sigma^{\mathrm{a}}_{12} = -\nabla^2\sigma^{\mathrm{a}}_{12} \\ &= -\frac{2R}{A}\nabla^2(Q_{11}H_{12} - Q_{12}H_{11}),\end{aligned} \tag{D18}$$

where $\epsilon_{\alpha\beta}$ denotes the Levi-Civita tensor.

The term coming from the Ericksen stress (symmetric in our case), defined in Eq. (D13), reads

$$\begin{aligned}\mathrm{curl}(\nabla\cdot\sigma^{\mathrm{E}}) &= \epsilon_{\gamma\alpha}\partial_\gamma\big(\partial_\beta\sigma^{\mathrm{E}}_{\alpha\beta}\big) \\ &= \partial_x\big(\partial_x\sigma^{\mathrm{E}}_{12} + \partial_y\sigma^{\mathrm{E}}_{22}\big) - \partial_y\big(\partial_x\sigma^{\mathrm{E}}_{11} + \partial_y\sigma^{\mathrm{E}}_{12}\big) \\ &= d_2\big(\sigma^{\mathrm{E}}_{22} - \sigma^{\mathrm{E}}_{11}\big) - 2d_1\sigma^{\mathrm{E}}_{12} \\ &= \frac{R}{A}\big(d_2((\partial_x Q_{11})^2 + (\partial_x Q_{12})^2 - (\partial_y Q_{11})^2 - (\partial_y Q_{12})^2) + 2d_1((\partial_x Q_{11})(\partial_y Q_{11}) + (\partial_x Q_{12})(\partial_y Q_{12}))\big).\end{aligned} \tag{D19}$$

Similarly, the term coming from the last (symmetric and trace-free) stress reads

$$\begin{aligned}\mathrm{curl}(\nabla\cdot\sigma) &= \epsilon_{\gamma\alpha}\partial_\gamma(\partial_\beta\sigma_{\alpha\beta}) \\ &= -2d_2\sigma_{11} - 2d_1\sigma_{12}.\end{aligned} \tag{D20}$$

It is convenient at this stage to decompose $\sigma = \sigma^{\mathrm{visc}} + \sigma^{\mathrm{act}} + \sigma^{\mathrm{align}}$ (respectively, the viscous, active, and flow-alignment stresses). Through Eqs. (D20) and (D14), we obtain

$$\begin{aligned}\mathrm{curl}(\nabla\cdot\sigma^{\mathrm{visc}}) &= -4\partial_y\partial_x v_{11} - 2\big(\partial_y^2 - \partial_x^2\big)v_{12} \\ &= -4\partial_y\partial_x^2 v_x - \big(\partial_y^2 - \partial_x^2\big)(\partial_x v_y + \partial_y v_x) \\ &= -4\partial_y^2\partial_x^2\psi - \big(\partial_y^2 - \partial_x^2\big)\big(-\partial_x^2\psi + \partial_y^2\psi\big) \\ &= -\big(\partial_x^4 + 2\partial_y^2\partial_x^2 + \partial_y^4\big)\psi = -\nabla^4\psi,\end{aligned} \tag{D21}$$

$$\mathrm{curl}(\nabla\cdot\sigma^{\mathrm{act}}) = 2S(d_2Q_{11} + d_1Q_{12}), \tag{D22}$$

$$\begin{aligned}\mathrm{curl}(\nabla\cdot\sigma^{\mathrm{align}}) &= -2d_2\sigma^{\mathrm{align}}_{11} - 2d_1\sigma^{\mathrm{align}}_{12} \\ &= -2\frac{Rv}{A}(d_2(H_{11} - 4Q_{11}(H_{11}Q_{11} + H_{12}Q_{12})) \\ &\quad + d_1(H_{12} - 4Q_{12}(H_{11}Q_{11} + H_{12}Q_{12}))).\end{aligned} \tag{D23}$$

Our problem for ψ is then given by

$$\nabla^4\psi = \text{(D18)} + \text{(D19)} + \text{(D22)} + \text{(D23)}, \tag{D24}$$

with the right-hand side fully explicit (i.e., independent on ψ).

With H_{11} and H_{12} defined in Eqs. (D9) and (D10), the reduced closed-form problem is given by Eqs. (D16), (D17), and (D24).

5. The θ model ($s = 1$ constraint)

To verify that our Q-tensor model is formulated consistently with respect to our constrained director-based model, we derive here the equations for $\partial_t\theta$ and ψ when the bulk term in $\mathbf{H}$ is replaced by a Lagrange multiplier that enforces $s = 1$.

When $s = 1$, we have

$$Q_{11} = \tfrac{1}{2}\cos 2\theta, \quad Q_{12} = \tfrac{1}{2}\sin 2\theta, \tag{D25}$$

where, as before, θ is the angle of the director $\boldsymbol{n}$ with respect to the x axis.

Now, the orientational field components are given by

$$H_{11} = \tfrac{1}{2}\nabla^2 Q_{11} + H_b^0 Q_{11} = -\tfrac{1}{2}\sin 2\theta \nabla^2\theta + \tfrac{1}{2}\cos 2\theta\big(H_b^0 - 2(\nabla\theta)^2\big), \quad \text{(D26)}$$

$$H_{12} = \tfrac{1}{2}\nabla^2 Q_{12} + H_b^0 Q_{12} = \tfrac{1}{2}\cos 2\theta \nabla^2\theta + \tfrac{1}{2}\sin 2\theta\big(H_b^0 - 2(\nabla\theta)^2\big), \quad \text{(D27)}$$

where H_b^0 is a Lagrange multiplier acting as a bulk forcing term.

Equation (D16) now reads

$$\begin{aligned} &-\sin 2\theta\left(\partial_t\theta + (\partial_y\psi, -\partial_x\psi)\cdot\nabla\theta + \frac{1}{2}\nabla^2\psi\right) \\ &= \frac{2}{A}\left(-\frac{1}{2}\sin 2\theta\nabla^2\theta + \frac{1}{2}\cos 2\theta\big(H_b^0 - 2(\nabla\theta)^2\big)\right) \\ &\quad - \nu((1-\cos^2 2\theta)d_2\psi - \cos 2\theta \sin 2\theta d_1\psi) \\ &= -\sin 2\theta\left(\frac{1}{A}\nabla^2\theta + \nu(\sin 2\theta\, d_2\psi - \cos 2\theta\, d_1\psi)\right) \\ &\quad + \cos 2\theta\frac{1}{A}\big(H_b^0 - 2(\nabla\theta)^2\big). \end{aligned} \quad \text{(D28)}$$

Similarly, Eq. (D17) now reads

$$\begin{aligned} &\cos 2\theta\left(\partial_t\theta + (\partial_y\psi, -\partial_x\psi)\cdot\nabla\theta + \frac{1}{2}\nabla^2\psi\right) \\ &= \frac{2}{A}\left(\frac{1}{2}\cos 2\theta\nabla^2\theta + \frac{1}{2}\sin 2\theta\big(H_b^0 - 2(\nabla\theta)^2\big)\right) \\ &\quad - \nu((1-\sin^2 2\theta)d_1\psi - \cos 2\theta \sin 2\theta d_2\psi) \\ &= \cos 2\theta\left(\frac{1}{A}\nabla^2\theta - \nu(\cos 2\theta\, d_1\psi - \sin 2\theta\, d_2\psi)\right) \\ &\quad + \sin 2\theta\frac{1}{A}\big(H_b^0 - 2(\nabla\theta)^2\big). \end{aligned} \quad \text{(D29)}$$

Applying a perpendicular projection

$$-\sin 2\theta\ \text{(D28)} + \cos 2\theta\ \text{(D29)},$$

we obtain

$$\begin{aligned} &\partial_t\theta + (\partial_y\psi, -\partial_x\psi)\cdot\nabla\theta + \frac{1}{2}\nabla^2\psi \\ &= \frac{1}{A}\nabla^2\theta - \nu(\cos 2\theta\, d_1\psi - \sin 2\theta\, d_2\psi). \end{aligned} \quad \text{(D30)}$$

From the parallel projection

$$\cos 2\theta\ \text{(D28)} + \sin 2\theta\ \text{(D29)},$$

we obtain

$$0 = H_b^0 - 2(\nabla\theta)^2. \quad \text{(D31)}$$

Thus, we recover in Eq. (D30) an equation for θ that is *identical* to Eq. (8). Unlike before, however, we find in Eq. (D31) that the Lagrange multiplier does not depend on flow, and the orientational field components simply reduce to

$$H_{11} = -\tfrac{1}{2}\sin 2\theta\,\nabla^2\theta, \quad H_{12} = \tfrac{1}{2}\cos 2\theta\,\nabla^2\theta.$$

Next, we turn to the curl of momentum balance [Eq. (D24)], where we aim to express each contribution on the RHS in terms of θ. From Eq. (D18), we obtain

$$\begin{aligned} \mathrm{curl}(\nabla\cdot\sigma^{\mathrm{a}}) &= -\frac{2R}{A}\nabla^2(Q_{11}H_{12} - Q_{12}H_{11}) \\ &= -\frac{R}{2A}\nabla^2(\cos^2 2\theta\nabla^2\theta + \sin^2 2\theta\nabla^2\theta) \\ &= -\frac{R}{2A}\nabla^4\theta. \end{aligned} \quad \text{(D32)}$$

From Eq. (D19), we obtain

$$\begin{aligned} \mathrm{curl}(\nabla\cdot\sigma^{\mathrm{E}}) &= \frac{R}{A}(d_2((\partial_x Q_{11})^2 + (\partial_x Q_{12})^2 - (\partial_y Q_{11})^2 \\ &\quad - (\partial_y Q_{12})^2) + 2d_1((\partial_x Q_{11})(\partial_y Q_{11}) \\ &\quad + (\partial_x Q_{12})(\partial_y Q_{12}))) \\ &= \frac{R}{A}(d_2((\partial_x\theta)^2 - (\partial_y\theta)^2) + 2d_1((\partial_x\theta)(\partial_y\theta))) \\ &= \frac{R}{A}((\partial_y\nabla^2\theta)\partial_x\theta - (\partial_x\nabla^2\theta)\partial_y\theta). \end{aligned} \quad \text{(D33)}$$

From Eq. (D22), we obtain

$$\begin{aligned} \mathrm{curl}(\nabla\cdot\sigma^{\mathrm{act}}) &= 2S(d_2 Q_{11} + d_1 Q_{12}) \\ &= S(d_2\cos 2\theta + d_1\sin 2\theta). \end{aligned} \quad \text{(D34)}$$

Finally, from Eq. (D23), we obtain

$$\begin{aligned} &\mathrm{curl}(\nabla\cdot\sigma^{\mathrm{align}}) \\ &= -2\frac{R\nu}{A}(d_2(H_{11} - 4Q_{11}(H_{11}Q_{11} + H_{12}Q_{12})) \\ &\quad + d_1(H_{12} - 4Q_{12}(H_{11}Q_{11} + H_{12}Q_{12}))) \\ &= -\frac{R\nu}{A}(-d_2(\sin 2\theta\,\nabla^2\theta) + d_1(\cos 2\theta\,\nabla^2\theta)). \end{aligned} \quad \text{(D35)}$$

We then have, via Eq. (D24),

$$\begin{aligned} \nabla^4\psi = {} & S(d_1\sin 2\theta + d_2\cos 2\theta) \\ & - \frac{R}{A}\left(\frac{1}{2}\nabla^4\theta + (\partial_x\nabla^2\theta)\partial_y\theta - (\partial_y\nabla^2\theta)\partial_x\theta \right. \\ & \left. + \nu(d_1(\cos 2\theta\,\nabla^2\theta) - d_2(\sin 2\theta\,\nabla^2\theta))\right). \end{aligned} \quad \text{(D36)}$$

This equation recovers the same form as Eq. (6), but with $h_\parallel = 0$—a consequence of the orthogonal form of flow alignment in the formulation of dynamics of $\mathbf{Q}$.

6. Numerical scheme

Here, we describe our pseudospectral method for numerically integrating Eq. (D24) and Eqs. (D16) and (D17). In what follows, the index n is the time iteration, dt is the time step, and $h = N^{-1}$ is the vertex spacing on our $N \times N$ square grid. We note that for defects to be adequately resolved, one must ensure that $h < \varepsilon$.

In the computations outlined below, all derivatives including $d_1 := \frac{1}{2}(\partial_y^2 - \partial_x^2)$, $d_2 := \partial_y\partial_x$ are performed in the space of the two-dimensional DFT. Before each real-space multiplication, we apply the 2/3 dealiasing rule, truncating the Fourier modes with $|q_x|$ or $|q_y|$ greater than $\frac{2}{3}\pi N$.

a. Computing current H components

We begin each iteration by computing H_{11}^n and H_{12}^n based on Q_{11}^n and Q_{12}^n, the arrays representing the current Q tensor on the vertices. Following Eqs. (D9) and (D10),

$$H_{11}^n = \tfrac{1}{2}\big(\nabla^2 Q_{11}^n + \varepsilon^{-2}(1-s^{n2})Q_{11}^n\big), \tag{D37}$$

$$H_{12}^n = \tfrac{1}{2}\big(\nabla^2 Q_{12}^n + \varepsilon^{-2}(1-s^{n2})Q_{12}^n\big), \tag{D38}$$

with

$$s^{n2} = 4\big({Q_{11}^n}^2 + {Q_{12}^n}^2\big).$$

b. Solving momentum balance

We turn to solving for the current streamfunction based on Q_{11}^n, Q_{12}^n and H_{11}^n, H_{12}^n. After rearranging terms in Eq. (D24), one has

$$\begin{aligned}\nabla^4\psi^n =\ & 2S\big(d_2 Q_{11}^n + d_1 Q_{12}^n\big)\\ &+ \frac{R}{A}\big(2\nabla^2\big(Q_{12}^n H_{11}^n - Q_{11}^n H_{12}^n\big)\\ &+ d_2\big(\big(\partial_x Q_{11}^n\big)^2 + \big(\partial_x Q_{12}^n\big)^2 - \big(\partial_y Q_{11}^n\big)^2 - \big(\partial_y Q_{12}^n\big)^2\big)\\ &+ 2d_1\big(\big(\partial_x Q_{11}^n\big)\big(\partial_y Q_{11}^n\big) + \big(\partial_x Q_{12}^n\big)\big(\partial_y Q_{12}^n\big)\big)\\ &- 2\nu\big(d_2\big(H_{11}^n - 4Q_{11}^n\big(H_{11}^n Q_{11}^n + H_{12}^n Q_{12}^n\big)\big)\\ &+ d_1\big(H_{12}^n - 4Q_{12}^n\big(H_{11}^n Q_{11}^n + H_{12}^n Q_{12}^n\big)\big)\big)\big).\end{aligned} \tag{D39}$$

Upon carefully computing all RHS contributions, this equation is trivially inverted in Fourier space,

$$\begin{aligned}&\mathcal{F}[\psi^n]_{\mathbf{q}} = \frac{1}{q^4}\mathcal{F}[\mathrm{RHS}^n]_{\mathbf{q}}, \quad \forall \mathbf{q} \neq \mathbf{0},\\ &\mathcal{F}[\psi^n]_{\mathbf{q}=\mathbf{0}} = 0.\end{aligned}$$

c. Computing the flow, vorticity, and additional flow gradients

Before attending to Eqs. (D16) and (D17), we truncate the highest 1/3 modes in ψ and compute the following fields pseudospectrally:

$$\begin{aligned}&v_x^n = \partial_y\psi^n, \quad v_y^n = -\partial_x\psi^n, \quad \omega^n = -\nabla^2\psi^n,\\ &E_1^n = d_1\psi^n, \quad E_2^n = d_2\psi^n.\end{aligned} \tag{D40}$$

d. Evolving Q components (integrating factor + Adams-Bashforth)

Let us rewrite Eqs. (D16) and (D17) with the linear Laplacian term stemming from $H_{\alpha\beta}$ moved to the LHS, along with the time derivative, and all other terms brought to the RHS.

$$\begin{aligned}\partial_t Q_{11} - \frac{1}{A}\nabla^2 Q_{11} =\ & \frac{1-s^2}{A\varepsilon^2}Q_{11} - (v_x, v_y)\cdot\nabla Q_{11} - \omega Q_{12}\\ &- \nu\big(\big(1-4Q_{11}^2\big)E_2 - 4Q_{11}Q_{12}E_1\big),\end{aligned} \tag{D41}$$

$$\begin{aligned}\partial_t Q_{12} - \frac{1}{A}\nabla^2 Q_{12} =\ & \frac{1-s^2}{A\varepsilon^2}Q_{12} - (v_x, v_y)\cdot\nabla Q_{12} + \omega Q_{11}\\ &- \nu\big(\big(1-4Q_{12}^2\big)E_1 - 4Q_{11}Q_{12}E_2\big),\end{aligned} \tag{D42}$$

where, as in Eq. (D40), $\omega = -\nabla^2\psi$, $E_1 = d_1\psi$, and $E_2 = d_2\psi$. Equations (D41) and (D42) are still expressed in continuous time. Upon time discretization, the terms on the RHS will be evaluated explicitly using a multistep method.

We now introduce the exponential integrating factor via a change of variable in Fourier space:

$$\hat{T}_{11}(\boldsymbol{q}, t) := \hat{Q}_{11}(\boldsymbol{q}, t)e^{A^{-1}q^2 t}.$$

It follows that

$$\begin{aligned}\partial_t\hat{T}_{11} &= e^{A^{-1}q^2 t}\left(\partial_t\hat{Q}_{11} + \frac{q^2}{A}\hat{Q}_{11}\right)\\ &= e^{A^{-1}q^2 t}\mathcal{F}[\mathrm{LHS(D41)}] = e^{A^{-1}q^2 t}\mathcal{F}[\mathrm{RHS(D41)}].\end{aligned}$$

We evolve $\hat{T}_{11}$ via the second-order Adams-Bashforth method (AB2),

$$\begin{aligned}\hat{T}_{11}^{n+1} =\ & \hat{T}_{11}^n + \frac{dt}{2}\big(3\,e^{A^{-1}q^2 t_n}\mathcal{F}[\mathrm{RHS}\,(\mathrm{D41})^n]\\ &- e^{A^{-1}q^2 t_{n-1}}\mathcal{F}[\mathrm{RHS(D41)}^{n-1}]\big),\end{aligned} \tag{D43}$$

where $\mathrm{RHS(D41)}^n$ denotes the right-hand side of Eq. (D41) evaluated at time t_n (with Q_{11}^n, Q_{12}^n, s^n, and v_x^n, v_y^n, ω^n, E_1^n, E_2^n), while $\mathrm{RHS(D41)}^{n-1}$ is evaluated at time t_{n-1} (with Q_{11}^{n-1}, Q_{12}^{n-1}, and so on).

Substituting the definition of $\hat{T}_{11}$ back in Eq. (D43), and dividing by $e^{A^{-1}q^2 t_{n+1}}$, we obtain

$$\begin{aligned}\hat{Q}_{11}^{n+1} =\ & \hat{Q}_{11}^n e^{-A^{-1}q^2 dt} + \frac{dt}{2}\big(3\,e^{-A^{-1}q^2 dt}\mathcal{F}[\mathrm{RHS(D41)}^n]\\ &- e^{-2A^{-1}q^2 dt}\mathcal{F}[\mathrm{RHS(D41)}^{n-1}]\big).\end{aligned} \tag{D44}$$

Applying the same procedure to Eq. (D42), we obtain

$$\begin{aligned}\hat{Q}_{12}^{n+1} =\ & \hat{Q}_{12}^n e^{-A^{-1}q^2 dt} + \frac{dt}{2}\big(3\,e^{-A^{-1}q^2 dt}\mathcal{F}[\mathrm{RHS(D42)}^n]\\ &- e^{-2A^{-1}q^2 dt}\mathcal{F}[\mathrm{RHS(D42)}^{n-1}]\big).\end{aligned} \tag{D45}$$

This concludes a single iteration of our explicit time-stepping scheme. The linear Laplacian term is treated exactly via an integrating factor, while all other terms are advanced explicitly using a second-order Adams-Bashforth method (AB2). All spatial derivatives are computed pseudospectrally and 2/3 dealiasing is applied prior to real-space multiplications. At the end of each iteration, we update not only Q_{11} and Q_{12}, but also the previous right-hand sides of Eqs. (D41) and (D42), as required for the AB2 scheme.

7. Agreement with the θ model at small ϵ/ℓ_a

In Fig. 11, we study the convergence of the full Q-tensor model to the $s = 1$ constrained, θ model (Appendix D 5) as the defect core size decreases. Specifically, we plot the spatial average of the squared deviation $|\mathbf{Q} - \boldsymbol{q}(\theta)|^2$ over time, with $\boldsymbol{q}(\theta)$ denoting the tensorial order parameter computed from the θ model simulation,

$$\boldsymbol{q}(\theta) = \frac{1}{2}\begin{pmatrix}\cos 2\theta & \sin 2\theta\\ \sin 2\theta & -\cos 2\theta\end{pmatrix}.$$

All simulations use the same parameters (except for ϵ) and the same initial condition: a nematic state with $s = 1$ and a small orientational perturbation. When true defects form ($\epsilon \gtrsim 0.3\ell_a$), decorrelation is reached rapidly as defects begin to

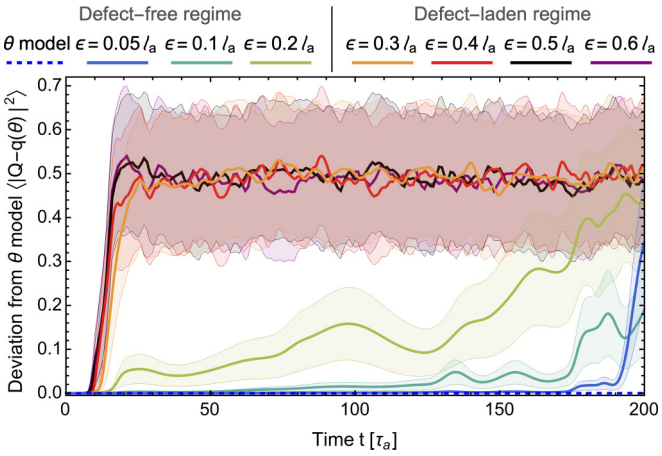

FIG. 11. Agreement with the constrained model at small defect core size. For all simulations shown in Fig. 7, which share the same initial conditions and parameters except for ϵ, we plot the space-averaged deviation of the nematic tensor $\mathbf{Q}$ from that corresponding to the reference θ model simulation. Shaded regions indicating the standard deviation. As ϵ decreases, quantitative agreement (low deviation) persists systematically for longer integration times. A deviation of $\sim$0.5 corresponds to complete statistical decorrelation. See also Movie S6 of the Supplemental Material [35].

nucleate. Below the nucleation threshold ($\epsilon \leqslant 0.2\ell_a$), the full Q-tensor simulations converge toward the constrained model for increasingly longer integration times as ϵ decreases. See Movie S6 of the Supplemental Material [35] for side by side evolutions.

8. Defect number, bulk energy, and elastic energy

In Fig. 12, we present time series and statistical breakdowns of the total defect number, bulk free energy, and elastic free energy from our Q-tensor simulations, as well as the constrained θ model for reference. This figure complements Fig. 7(b), which, for compactness, shows only the time-averaged values of these quantities.

The total defect count [Fig. 12(a)] sums over both $+1/2$ and $-1/2$ defects, identified using a thresholding method detailed in Appendix E 3. Near the transition from arrested wall networks to defect-laden turbulence, we find that the total number of defects (at long times) increases sharply with the ratio ϵ/ℓ_s. Interestingly, this number—proportional to the defect density since the system size is fixed—shows a non-monotonic dependence on ϵ. Understanding the origin of the observed decrease in defect density with increasing core size is deferred to future work.

We note that the total bulk free energy [Fig. 12(b)] is computed relative to the minimum at $s = 1$, which differs for each value of ϵ. The variations in this energy across the simulations are, in absolute terms, much smaller than the variations observed in the elastic free energy [Fig. 12(c)].

APPENDIX E: IMAGE PROCESSING

1. Skeleton detection and pseudodefect classification

The process of skeleton detection and pseudodefect classification is depicted in Fig. 13. We apply the following pipeline using the image processing tools in Mathematica (TM).

Initially, a plot of the Frank free energy density, $|\nabla\theta|^2$, is rendered [Fig. 13(a)]. The gray-scale color scheme and the plot range are chosen to aid the binarization of the walls. To avoid false node detection along the square boundaries, this plot is periodically expanded using the **ImageAssemble** function [Fig. 13(b)]. Subsequently, we binarize the image by applying the **LocalAdaptiveBinarize** function, with neighbourhood pixel range set to 6. Then, we apply the **DeleteSmallComponents** function to remove isolated white domains, specified as totalling 20 or fewer pixels, that we do not consider part of the wall network [Fig. 13(c)].

To obtain the network skeleton, we apply the **Thinning** function with default setting on the binarized image. At times, this alone can leave tiny black gaps within some walls that would later be falsely interpreted as branching points. To avoid this, we further apply the **Dilation** function, with range set to 1 pixel, and then repeat **Thinning**. To prune short branches from the skeleton, we apply the **Pruning** function, specifying the range to 2 pixels. The final skeleton is shown in Fig. 13(d).

The nodes of the skeleton are then detected using the **MorphologicalTransform** function, specifying "SkeletonBranchPoints" and then "SkeletonEndPoints" [highlighted in blue and red, respectively, in Fig. 13(e)]. The nodes are filtered to retain only those within the original square [Fig. 13(f)]. At this stage, the "SkeletonBranchPoints" correspond to our pseudodefect branchpoints [Fig. 3(b)]. However, the "SkeletonEndPoints" can be either pseudodefect endpoints [Fig. 3(c)] or startpoints [Fig. 3(a)].

To distinguish between endpoints and startpoints, we test whether the wall polarity faces outward or inward with respect to the branch associated with each "SkeletonEndPoint." To this end, we compute two vectors on each such node. The vector pointing outward from the associated branch is calculated by locating the nearest neighboring point on the wall skeleton [Fig. 13(g)]. The wall polarity at each node is determined by $(\partial_y\theta, -\partial_x\theta)$. The scalar product of the polarity with the outward vector classifies the type of pseudodefect [Fig. 13(h)].

Finally, Fig. 13(i) displays the classified nodes with branchpoints (blue), endpoints (red), and startpoints (green)—all oriented according to the local wall polarity.

2. Labyrinths detection

The process of labyrinth detection in arrested wall networks is depicted in Fig. 14. Here, the frames of interest are those in which no startpoints have been detected. Similarly to our skeleton detection scheme, we apply a pipeline that uses the image processing tools in Mathematica (TM).

Initially, an inverted plot of $|\nabla\theta|^2$ is rendered [Fig. 14(a)]. The color scheme and plot range are selected to aid the binarization of the gaps between the walls. To assist in identifying connected domains that frequently pass through the square boundaries, this plot is periodically expanded using the **ImageAssemble** function [Fig. 14(b)]. The **LocalAdaptiveBinarize** function is then applied with a neighborhood pixel range set to 10, followed by the **FillingTransform** function to eliminate isolated black fragments not considered as walls [Fig. 14(c)].

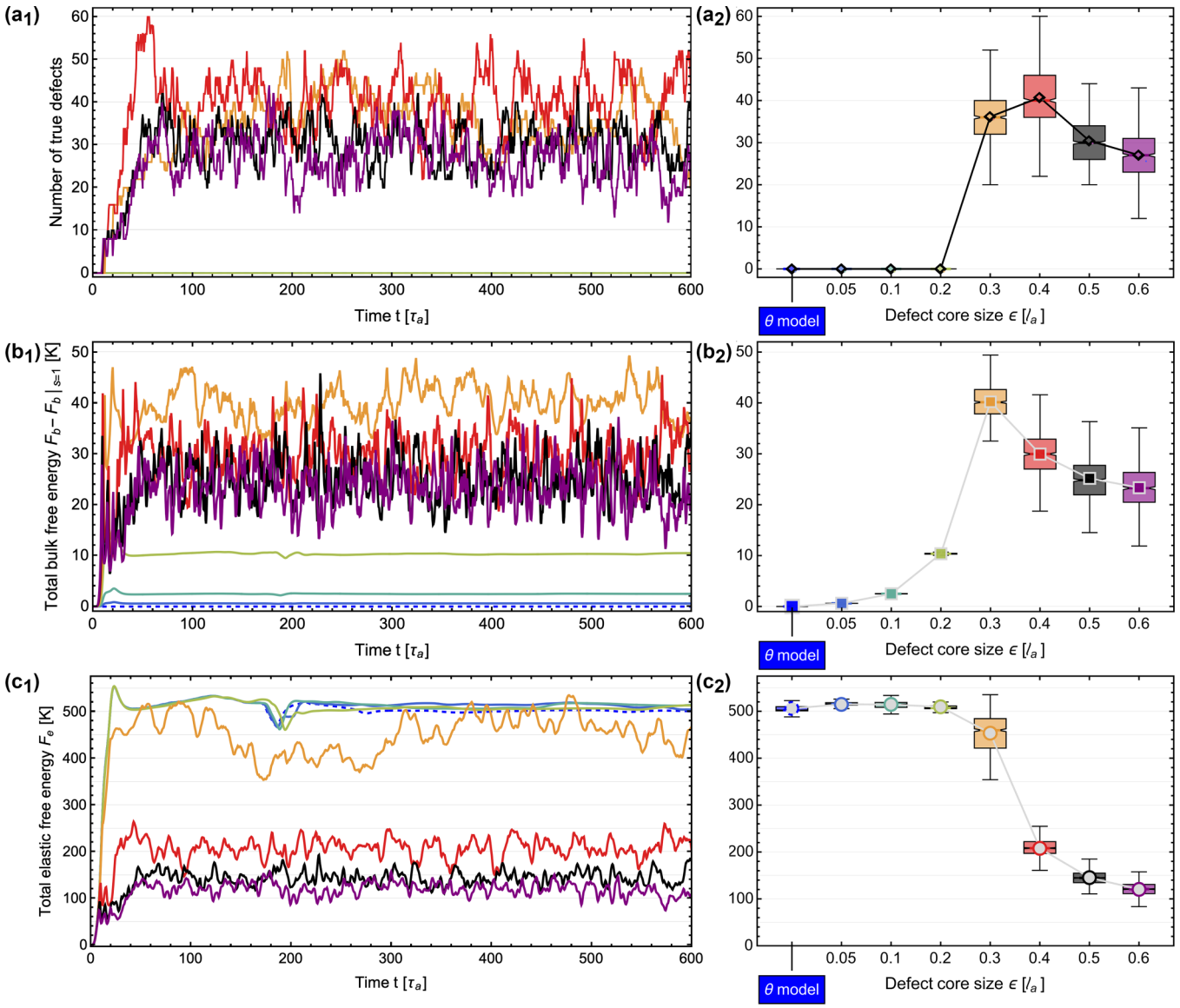

FIG. 12. Time series and statistical breakdown of the total defect number and free energy contributions. (a_1) Number of true topological defects as a function of time in simulations where ϵ is the varied control parameter. Colors correspond to the ϵ values in Figs. 7 and 11. For $\epsilon \leqslant 0.2\,\ell_a$, the system does not spontaneously form defects. (a_2) Box-whisker plot summarizing the data in panel (a_1) for $t > 100\,\tau a$ (excluding initial transients), as a function of ϵ. The boxes span the interquartile range (25%–75%), with notches indicating the median and whiskers showing the upper and lower fences. Diamond markers connected by a black line denote the mean values, also shown in Fig. 7(b). (b_1) Total bulk free energy, computed relative to its minimum at $s = 1$, shown as a function of time for each simulation. Colors indicate the value of ϵ and the dashed blue curve (here identically zero) represents the θ model. (b_2) Same as panel (a_2) for the data in panel (b_1). Square markers connected by a gray line denote the mean values, also shown in Fig. 7(b). (c_1) Total elastic free energy shown as a function of time for each simulation. Again, colors indicate the value of ϵ and the dashed blue curve represents the θ model. (c_2) Same as panel (a_2) for the data in panel (c_1). Circle markers connected by a gray line denote the mean values, also shown in Fig. 7(b). Note the difference in scales between variations in panel (c) vs panel (b).

Next, we find the connected morphological domains in the binarized image using the **MorphologicalComponents** function [Fig. 14(d)]. These distinctly labeled domains are then cropped to retain only those within the original periodic square [Fig. 14(e)].

To relabel domains that connect through the left-right and top-bottom boundaries, we employ a custom algorithm that ensures continuity across the periodic square [Fig. 14(f)]. This step completes the process of detecting the unicursal labyrinths that span the system size.

3. Topological defects detection

The detection of true defects is more straightforward than that of pseudodefects, since the tensorial order parameter $\mathbf{Q}$ provides clear local signatures of their appearance. Specifically, we rely on the scalar order parameter $s = 2\sqrt{Q_{11}^2 + Q_{12}^2}$ and the so-called topological defect density:

$$\rho_{\text{top}} = \frac{1}{\pi}(\partial_x Q_{11}\partial_y Q_{12} - \partial_y Q_{11}\partial_x Q_{12}).$$

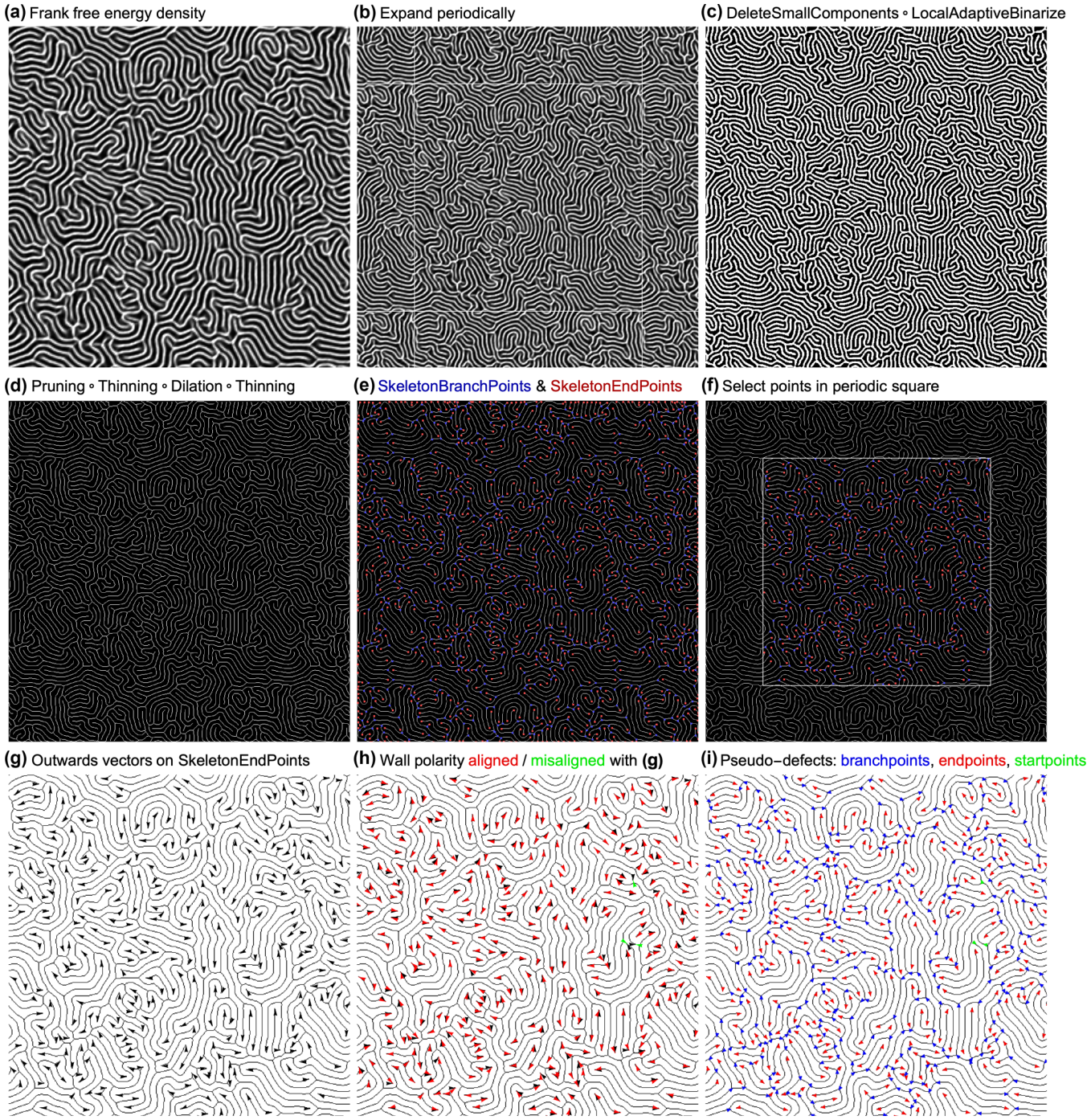

FIG. 13. Skeleton detection and pseudodefect classification. (a) Gray-scale plot of the Frank free energy density, with black corresponding to $|\nabla\theta|^2 = 0$ and white corresponding to $|\nabla\theta|^2 \geqslant 0.5\,\max|\nabla\theta|^2$ to facilitate binarization. (b) Periodic expansion of panel (a) to avoid false detection of nodes along the original square boundaries (white outline). (c) Local adaptive binarization of panel (b), followed by removal of small fragmented components not counted as walls. (d) Recursive thinning of panel (c), then a step of dilation to fill up tiny gaps within some walls, an additional thinning step to recover the skeleton, and a pruning step to discard open branches shorter than a small threshold. (e) Using the MorphologicalTransform tool, we detect and highlight the skeleton nodes. (f) We select only those nodes confined to the original periodic square. (g) For the SkeletonEndPoints, we compute the vectors pointing outward of their associated branch (black arrows) by finding the nearest neighboring point on the wall skeleton. (h) The wall polarity associated with each SkeletonEndPoint is shown in red (green) if its scalar product with panel (g) is positive (negative). (i) Branchpoints (blue nodes), endpoints (red nodes), and startpoints (green nodes) are plotted with their orientation given by the local wall polarity.

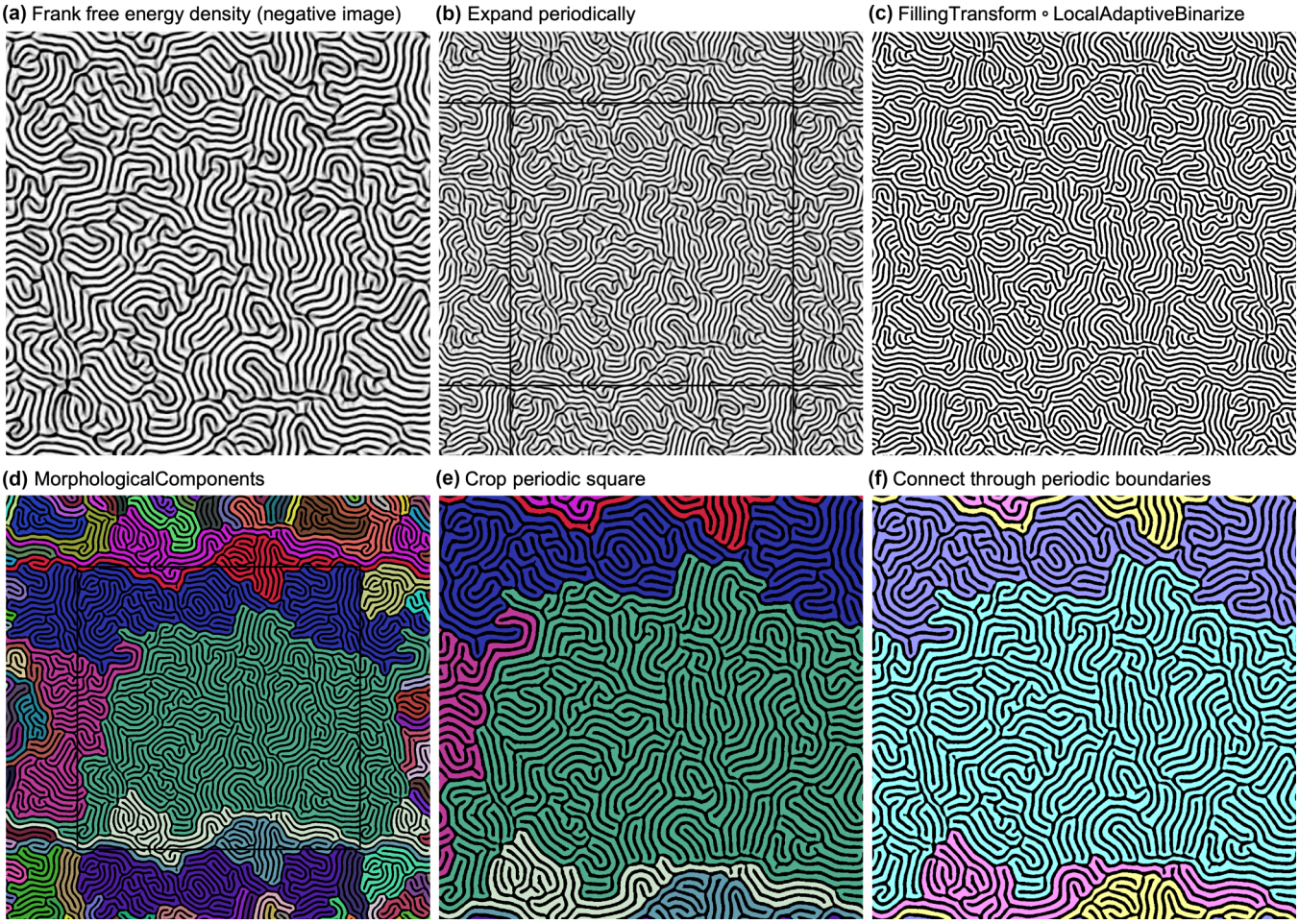

FIG. 14. Labyrinths detection in arrested wall networks. (a) Gray-scale plot of the Frank free energy density, with white corresponding to $|\nabla\theta|^2 = 0$ and black corresponding to $|\nabla\theta|^2 \geqslant 0.5 \max|\nabla\theta|^2$ to facilitate binarization. (b) Periodic expansion of panel (a) to capture connected domains that meander through the periodic square boundaries. (c) Local adaptive binarization of panel (b), followed by a filling operator to discard isolated black fragments. (d) Finding the connected morphological domains in panel (c). (e) Cropping out the periodic square domain from panel (d). (f) Applying our algorithm for relabeling domains that are connected through the left-right and top-bottom boundaries.

At a defect core, s falls to low values, approaching zero in the continuum limit, while ρ_{top} develops local extrema whose sign indicates the topological charge. We identified core regions using a thresholding approach: a vertex was marked as part of a $+1/2$ defect core if $s < s_0$ and $\rho_{\text{top}} > r_0 \max(\rho_{\text{top}})$, and as part of a $-1/2$ defect core if $s < s_0$ and $\rho_{\text{top}} < r_0 \min(\rho_{\text{top}})$, with $0 < s_0 < 1$ and $0 < r_0 < 1$ as threshold parameters.

For each frame, we generated two binarized images based on these criteria and tiled them across periodic boundaries to obtain an added margin. Using the **ComponentMeasurements** function, we extracted centroids of connected regions, corresponding to the locations of positive and negative defect cores. We then filtered these to retain only those centroids that lie within the original simulation domain. We explored several values of s_0 and r_0 to achieve the closest agreement between the counts of $+1/2$ and $-1/2$ defects, as required by topological charge conservation. The detected defect positions were overlaid on plots of the director field (computed as the eigenvector of $\mathbf{Q}$) to visually confirm the results.

APPENDIX F: SUPPLEMENTAL MOVIE CAPTIONS

Movie S1: Strong large-scale turbulence in the contractile aligning regime. The left panel shows the evolution of the flow field $\boldsymbol{v}$, with color indicating speed and black arrows representing streamlines. The right panel depicts the evolution of the Frank free energy density, $|\nabla\theta|^2$. The parameters are the same as in Figs. 1(a) and 1(b), which are snapshots from the same simulation. The interval between movie frames is 500 computational time iterations, corresponding to a time interval of $5\tau_a$. The total duration of the movie is $2500\tau_a$.

Movie S2: Arrested turbulence in the extensile aligning regime. The left panel shows the evolution of the flow field $\boldsymbol{v}$, with color indicating speed and black arrows representing streamlines. The right panel depicts the evolution of the Frank free energy density, $|\nabla\theta|^2$. The parameters are the same as in Figs. 1(d) and 1(e), which are snapshots from the same simulation. The interval between movie frames is 500 computational time iterations, corresponding to a time interval of $5\tau_a$. The total duration of the movie is $2500\tau_a$.

Movie S3: Active turbulence in the absence of flow alignment (tumbling regime). The left panel shows the evo-

lution of the flow field $\boldsymbol{v}$, with color indicating speed and black arrows representing streamlines. The right panel depicts the evolution of the Frank free energy density, $|\nabla\theta|^2$. The parameters are the same as in Fig. S1 of the Supplemental Material [35], showing snapshots from the same simulation. The interval between movie frames is 500 computational time iterations, corresponding to a time interval of $5\tau_a$. The total duration of the movie is $2500\tau_a$.

Movie S4: Evolution from stripes to turbulence (contractile aligning versus extensile aligning). The evolution of the Frank free energy density, $|\nabla\theta|^2$, in the contractile aligning case ($S\nu = +1.1$, left) and the extensile aligning case ($S\nu = -1.1$, right). The wavelength of the initial stripes—with splay walls on the left and bend walls on the right—was chosen to match the selected wavelength in the fully developed turbulent state. In both cases, the stripes coarsen and then experience a "zigzag" instability that folds the walls. In the contractile case (left), folded walls tend to dissolve and reappear perpetually. In the extensile case (right, Fig. 2), walls are more robust and tend to branch. As growing branches avoid other walls, the system reaches a gridlocked state that fluctuates only slightly. Parameters were set to $R = 1$, $\nu = -1.1$, and $A = 19692$ (chosen so that the system size roughly equals six times the selected wavelength). The interval between movie frames is 50 computational time iterations, corresponding to a time interval of $1\tau_a$. The total duration of the movie is $540\tau_a$.

Movie S5: Evolution of the wall-network skeleton and its nodes. Skeleton of the domain walls (black) with startpoints, branchpoints, and endpoints shown as green, blue, and red triangular nodes, respectively (see Fig. 3). The detection of these structures is described in Appendix E and Fig. 13. This movie demonstrates the pseudotopological transitions mediating the ageing of an arrested wall network. Parameter values are as in Fig. 5. The interval between movie frames is 500 computational time iterations, corresponding to a time interval of $5\tau_a$. The total duration of the movie is $1715\tau_a$.

Movie S6: Agreement between the constrained θ model and the unconstrained Q-tensor model at low defect core size. Evolution of the flow (top panels) and the elastic energy density (bottom panels) in the θ model, compared with the Q-tensor model at low values of ϵ. The behavior of the latter converges to the constrained case as ϵ decreases relative to ℓ_a. See also Figs. 7 and 11. Other parameters were set to $R = 1$, $\nu = -1$, $S = 1$, and $A = 10^4$. The interval between movie frames is 500 computational time iterations, corresponding to a time interval of $0.5\tau_a$. The total duration of the movie is $220\tau_a$.

Movie S7: Transition from dynamical arrest to defect-laden turbulence. Evolution of the flow (top panels) and the elastic energy density (bottom panels) in the Q-tensor model, with ϵ varied across the defect proliferation threshold. See also Fig. 7. Other parameters were set to $R = 1$, $\nu = -1$, $S = 1$, and $A = 10^4$. The interval between movie frames is 200 computational time iterations, corresponding to a time interval of $1\tau_a$. The total duration of the movie is $600\tau_a$.

Movie S8: Unraveling dynamical arrest via a core-size quench. The left panel shows the elastic energy density, and the right panel shows a line-integral-convolution plot of the director, overlaid with the scalar order parameter (black indicating $s \to 0$). We first present the evolution of an arrested state generated at a low defect core size ($\epsilon = 0.2\ell_a$). We then pause to highlight the localized energy peaks associated with branchpoint pseudodefects. Next, the simulation is continued with a larger defect core size, beyond the threshold for defect nucleation ($\epsilon = 0.35\ell_a$), showing that defect pairs nucleate at suspected hot spots. Finally, we replay the last segment with the true defects explicitly traced: Yellow points are $+1/2$ defects, while cyan points are $-1/2$ defects. Other parameters were set to $R = 1$, $\nu = -1$, $S = 1$, and $A = 10^4$.

Movie S9: Enlarged defect-free extensile system. Evolution of the elastic energy density from simulations of the constrained θ model (Appendix D 5) in the extensile, rod-aligning regime ($S\nu = -1.1$). For reference, the movie begins with activity $A = 3.2 \times 10^5$ on a 256×256 grid, as in Fig. 1, where the system rapidly develops an arrested state with persistent labyrinths spanning the entire domain. It then shows a larger system with $A = 5.12 \times 10^6$ on a 1024×1024 grid, where more extensive labyrinths form but are frequently fractured, preventing persistent system-spanning connectivity.

Movie S10: Enlarged defect-free contractile system. Evolution of the elastic energy density from simulations of the constrained θ model (Appendix D 5) in the contractile, rod-aligning regime ($S\nu = +1.1$). The movie begins with activity $A = 3.2 \times 10^5$ on a 256×256 grid, as in Fig. 1. It then shows a larger system with $A = 5.12 \times 10^6$ on a 1024×1024 grid.

APPENDIX G: SUPPLEMENTAL ANIMATION CAPTIONS

Animation S1: Startpoint-endpoint pair birth and annihilation via wall inception and wall dissolution. This animation illustrates both the forward and inverse processes related to Fig. 3(d).

Animation S2: Endpoint-startpoint pair birth and annihilation via local wall deletion and wall completion. This animation illustrates both the forward and inverse processes related to Fig. 3(e).

Animation S3: Branchpoint-endpoint pair birth and annihilation via wall branching and wall retraction. This animation illustrates both the forward and inverse processes related to Fig. 3(f).

Animation S4: Branchpoint to startpoint transition by wall disjoining and startpoint to branchpoint transition by wall joining. This animation illustrates both the forward and inverse processes related to Fig. 3(g).

Animation S5: T1 transitions of connected branchpoints. This animation illustrates both the forward and inverse processes related to Fig. 3(h).

[1] R. Alert, J. Casademunt, and J.-F. Joanny, Active turbulence, Annu. Rev. Condens. Matter Phys. **13**, 143 (2022).

[2] C. Dombrowski, L. Cisneros, S. Chatkaew, R. E. Goldstein, and J. O. Kessler, Self-concentration and large-scale

coherence inbacterial dynamics, Phys. Rev. Lett. **93**, 098103 (2004).
[3] L. H. Cisneros, R. Cortez, C. Dombrowski, R. E. Goldstein, and J. O. Kessler, Fluid dynamics of self-propelled microorganisms, from individuals to concentrated populations, Exp. Fluids **43**, 737 (2007).
[4] T. Ishikawa, N. Yoshida, H. Ueno, M. Wiedeman, Y. Imai, and T. Yamaguchi, Energy transport in a concentrated suspension of bacteria, Phys. Rev. Lett. **107**, 028102 (2011).
[5] H. H. Wensink, J. Dunkel, S. Heidenreich, K. Drescher, R. E. Goldstein, H. Löwen, and J. M. Yeomans, Meso-scale turbulence in living fluids, Proc. Natl. Acad. Sci. USA **109**, 14308 (2012).
[6] J. Dunkel, S. Heidenreich, K. Drescher, H. H. Wensink, M. Bär, and R. E. Goldstein, Fluid dynamics of bacterial turbulence, Phys. Rev. Lett. **110**, 228102 (2013).
[7] A. E. Patteson, A. Gopinath, and P. E. Arratia, The propagation of active-passive interfaces in bacterial swarms, Nat. Commun. **9**, 5373 (2018).
[8] H. Li, X.-Q. Shi, M. Huang, X. Chen, M. Xiao, C. Liu, H. Chaté, and H. P. Zhang, Data-driven quantitative modeling of bacterial active nematics, Proc. Natl. Acad. Sci. USA **116**, 777 (2019).
[9] Y. Peng, Z. Liu, and X. Cheng, Imaging the emergence of bacterial turbulence: Phase diagram and transition kinetics, Sci. Adv. **7**, eabd1240 (2021).
[10] Z. Liu, W. Zeng, X. Ma, and X. Cheng, Density fluctuations and energy spectra of 3D bacterial suspensions, Soft Matter **17**, 10806 (2021).
[11] D. Wei, Y. Yang, X. Wei, R. Golestanian, M. Li, F. Meng, and Y. Peng, Scaling transition of active turbulence from two to three dimensions, Adv. Sci. **11**, 2402643 (2024).
[12] A. Creppy, O. Praud, X. Druart, P. L. Kohnke, and F. Plouraboué, Turbulence of swarming sperm, Phys. Rev. E **92**, 032722 (2015).
[13] T. Sanchez, D. T. N. Chen, S. J. DeCamp, M. Heymann, and Z. Dogic, Spontaneous motion in hierarchically assembled active matter, Nature (London) **491**, 431 (2012).
[14] G. Henkin, S. J. DeCamp, D. T. N. Chen, T. Sanchez, and Z. Dogic, Tunable dynamics of microtubule-based active isotropic gels, Philos. Trans. R. Soc. A **372**, 20140142 (2014).
[15] P. Guillamat, J. Ignés-Mullol, and F. Sagués, Taming active turbulence with patterned soft interfaces, Nat. Commun. **8**, 564 (2017).
[16] P. W. Ellis, D. J. G. Pearce, Y.-W. Chang, G. Goldsztein, L. Giomi, and A. Fernandez-Nieves, Curvature-induced defect unbinding and dynamics in active nematic toroids, Nat. Phys. **14**, 85 (2018).
[17] N. Kumar, R. Zhang, J. J. de Pablo, and M. L. Gardel, Tunable structure and dynamics of active liquid crystals, Sci. Adv. **4**, eaat7779 (2018).
[18] L. M. Lemma, S. J. DeCamp, Z. You, L. Giomi, and Z. Dogic, Statistical properties of autonomous flows in 2D active nematics, Soft Matter **15**, 3264 (2019).
[19] B. Martínez-Prat, J. Ignés-Mullol, J. Casademunt, and F. Sagués, Selection mechanism at the onset of active turbulence, Nat. Phys. **15**, 362 (2019).
[20] A. J. Tan, E. Roberts, S. A. Smith, U. A. Olvera, J. Arteaga, S. Fortini, K. A. Mitchell, and L. S. Hirst, Topological chaos in active nematics, Nat. Phys. **15**, 1033 (2019).
[21] G. Duclos, R. Adkins, D. Banerjee, M. S. E. Peterson, M. Varghese, I. Kolvin, A. Baskaran, R. A. Pelcovits, T. R. Powers, A. Baskaran, F. Toschi, M. F. Hagan, S. J. Streichan, V. Vitelli, D. A. Beller, and Z. Dogic, Topological structure and dynamics of three-dimensional active nematics, Science **367**, 1120 (2020).
[22] B. Martínez-Prat, R. Alert, F. Meng, J. Ignés-Mullol, J.-F. Joanny, J. Casademunt, R. Golestanian, and F. Sagués, Scaling regimes of active turbulence with external dissipation, Phys. Rev. X **11**, 031065 (2021).
[23] A. Doostmohammadi, S. P. Thampi, T. B. Saw, C. T. Lim, B. Ladoux, and J. M. Yeomans, Cell division: A source of active stress in cellular monolayers, Soft Matter **11**, 7328 (2015).
[24] T. D. Yang, H. Kim, C. Yoon, S.-K. Baek, and K. J. Lee, Collective pulsatile expansion and swirls in proliferating tumor tissue, New J. Phys. **18**, 103032 (2016).
[25] C. Blanch-Mercader, V. Yashunsky, S. Garcia, G. Duclos, L. Giomi, and P. Silberzan, Turbulent dynamics of epithelial cell cultures, Phys. Rev. Lett. **120**, 208101 (2018).
[26] S.-Z. Lin, W.-Y. Zhang, D. Bi, B. Li, and X.-Q. Feng, Energetics of mesoscale cell turbulence in two-dimensional monolayers, Commun. Phys. **4**, 21 (2021).
[27] X. Li, S. Sinha, T. R. Kirkpatrick, and D. Thirumalai, Topological transitions, turbulent-like motion and long-time-tails driven by cell division in biological tissues, arXiv:2211.14410.
[28] D. Nishiguchi and M. Sano, Mesoscopic turbulence and local order in Janus particles self-propelling under an ac electric field, Phys. Rev. E **92**, 052309 (2015).
[29] G. Kokot, S. Das, R. G. Winkler, G. Gompper, I. S. Aranson, and A. Snezhko, Active turbulence in a gas of self-assembled spinners, Proc. Natl. Acad. Sci. USA **114**, 12870 (2017).
[30] H. Karani, G. E. Pradillo, and P. M. Vlahovska, Tuning the random walk of active colloids: From individual run-and-tumble to dynamic clustering, Phys. Rev. Lett. **123**, 208002 (2019).
[31] M. Bourgoin, R. Kervil, C. Cottin-Bizonne, F. Raynal, R. Volk, and C. Ybert, Kolmogorovian active turbulence of a sparse assembly of interacting Marangoni surfers, Phys. Rev. X **10**, 021065 (2020).
[32] L. Giomi, Geometry and topology of turbulence in active nematics, Phys. Rev. X **5**, 031003 (2015).
[33] R. Alert, J.-F. Joanny, and J. Casademunt, Universal scaling of active nematic turbulence, Nat. Phys. **16**, 682 (2020).
[34] C. Rorai, F. Toschi, and I. Pagonabarraga, Coexistence of active and hydrodynamic turbulence in two-dimensional active nematics, Phys. Rev. Lett. **129**, 218001 (2022).
[35] See Supplemental Material at http://link.aps.org/supplemental/10.1103/1jyc-t1z4 for the Supplemental Figs. S1–S4.
[36] P.-G. de Gennes and J. Prost, *The Physics of Liquid Crystals*, 2nd ed. (Oxford University Press, New York, 1993).
[37] F. Jülicher, S. W. Grill, and G. Salbreux, Hydrodynamic theory of active matter, Rep. Prog. Phys. **81**, 076601 (2018).
[38] I. Lavi, R. Alert, J.-F. Joanny, and J. Casademunt, Nonlinear spontaneous flow instability in active nematics, Phys. Rev. Lett. **134**, 238301 (2025).
[39] K. Kruse, J. F. Joanny, F. Jülicher, J. Prost, and K. Sekimoto, Generic theory of active polar gels: A paradigm for cytoskeletal dynamics, Eur. Phys. J. E **16**, 5 (2005).
[40] M. C. Marchetti, J. F. Joanny, S. Ramaswamy, T. B. Liverpool, J. Prost, M. Rao, and R. A. Simha, Hydrodynamics of soft active matter, Rev. Mod. Phys. **85**, 1143 (2013).

[41] J. Prost, F. Jülicher, and J.-F. Joanny, Active gel physics, Nat. Phys. **11**, 111 (2015).
[42] S. A. Edwards and J. M. Yeomans, Spontaneous flow states in active nematics: A unified picture, Europhys. Lett. **85**, 18008 (2009).
[43] L. Giomi, M. J. Bowick, P. Mishra, R. Sknepnek, and M. Cristina Marchetti, Defect dynamics in active nematics, Philos. Trans. A. Math. Phys. Eng. Sci. **372**, 20130365 (2014).
[44] S. P. Thampi, R. Golestanian, and J. M. Yeomans, Instabilities and topological defects in active nematics, Europhys. Lett. **105**, 18001 (2014).
[45] S. P. Thampi, R. Golestanian, and J. M. Yeomans, Vorticity, defects and correlations in active turbulence, Philos. Trans. R. Soc. A Math. Phys. Eng. Sci. **372**, 20130366 (2014).
[46] S.P. Thampi and J.M. Yeomans, Active turbulence in active nematics, Eur. Phys. J. Spec. Top. **225**, 651 (2016).
[47] R. Voituriez, J. F. Joanny, and J. Prost, Spontaneous flow transition in active polar gels, Europhys. Lett. **70**, 404 (2005).
[48] R. Ramaswamy and F. Jülicher, Activity induces traveling waves, vortices and spatiotemporal chaos in a model actomyosin layer, Sci. Rep. **6**, 20838 (2016).
[49] P. A. M. Dirac, Quantised singularities in the electromagnetic field, Proc. R. Soc. A Math. Phys. Eng. Sci. **133**, 60 (1931).
[50] P. Chandrakar, M. Varghese, S. A. Aghvami, A. Baskaran, Z. Dogic, and G. Duclos, Confinement controls the bend instability of three-dimensional active liquid crystals, Phys. Rev. Lett. **125**, 257801 (2020).
[51] P. Guillamat, J. Ignés-Mullol, and F. Sagués, Control of active liquid crystals with a magnetic field, Proc. Natl. Acad. Sci. USA **113**, 5498 (2016).
[52] S. J. DeCamp, G. S. Redner, A. Baskaran, M. F. Hagan, and Z. Dogic, Orientational order of motile defects in active nematics, Nat. Mater. **14**, 1110 (2015).
[53] L. M. Lemma, M. M. Norton, A. M. Tayar, S. J. DeCamp, S. A. Aghvami, S. Fraden, M. F. Hagan, and Z. Dogic, Multiscale microtubule dynamics in active nematics, Phys. Rev. Lett. **127**, 148001 (2021).
[54] A. Ardaševa, I. Vélez-Cerón, M. C. Pedersen, J. Ignés-Mullol, F. Sagués, and A. Doostmohammadi, Beyond dipolar activity: Quadrupolar stress drives collapse of nematic order on frictional substrates, Phys. Rev. Lett. **134**, 088301 (2025).
[55] B. Li, K. Lou, W. Kob, and S. Granick, Anatomy of cage formation in a two-dimensional glass-forming liquid, Nature (London) **587**, 225 (2020).
[56] C. Patrick Royall, S. R. Williams, T. Ohtsuka, and H. Tanaka, Direct observation of a local structural mechanism for dynamic arrest, Nat. Mater. **7**, 556 (2008).
[57] C. Patrick Royall and S. R. Williams, The role of local structure in dynamical arrest, Phys. Rep. **560**, 1 (2015).
[58] J. Billock, Walk the world's most meditative labyrinths, Smithsonian Magazine, 2016, https://www.smithsonianmag.com/travel/walk-worlds-meditative-labyrinths-180957823/.
[59] https://commons.wikimedia.org/w/index.php?curid=5111302
[60] CC BY-SA 3.0, https://creativecommons.org/licenses/by-sa/3.0/deed.en.
[61] Metropolitan Museum of Art, https://www.metmuseum.org/art/collection/search/254598
[62] I. Bordeu, M. G. Clerc, R. Lefever, and M. Tlidi, From localized spots to the formation of invaginated labyrinthine structures in a Swift-Hohenberg model, Commun. Nonlinear Sci. Numer. Simul. **29**, 482 (2015).
[63] M. Seul, L. R. Monar, L. O. Gorman, and R. Wolfe, Morphology and local structure in labyrinthine stripe domain phase, Science **254**, 1616 (1991).
[64] M. Seul, L. R. Monar, and L. O'Gorman, Pattern analysis of magnetic stripe domains morphology and topological defects in the disordered state, Philos. Mag. B **66**, 471 (1992).
[65] B. Reimann, R. Richter, and I. Rehberg, Glasslike relaxation of labyrinthine domain patterns, Phys. Rev. E **65**, 031504 (2002).
[66] D. Marenduzzo, E. Orlandini, and J. M. Yeomans, Hydrodynamics and rheology of active liquid crystals: A numerical investigation, Phys. Rev. Lett. **98**, 118102 (2007).
[67] S. P. Thampi, R. Golestanian, and J. M. Yeomans, Velocity correlations in an active nematic, Phys. Rev. Lett. **111**, 118101 (2013).
[68] A. Doostmohammadi, M. F. Adamer, S. P. Thampi, and J. M. Yeomans, Stabilization of active matter by flow-vortex lattices and defect ordering, Nat. Commun. **7**, 10557 (2016).
[69] E. J. Hemingway, P. Mishra, M. Cristina Marchetti, and S. M. Fielding, Correlation lengths in hydrodynamic models of active nematics, Soft Matter **12**, 7943 (2016).
[70] C. Rorai, F. Toschi, and I. Pagonabarraga, Active nematic flows confined in a two-dimensional channel with hybrid alignment at the walls: A unified picture, Phys. Rev. Fluids **6**, 113302 (2021).
[71] L. C. Head, C. Doré, R. R. Keogh, L. Bonn, G. Negro, D. Marenduzzo, A. Doostmohammadi, K. Thijssen, T. López-León, and T. N. Shendruk, Spontaneous self-constraint in active nematic flows, Nat. Phys. **20**, 492 (2024).
[72] A. N. Beris and B. J. Edwards, *Thermodynamics of Flowing Systems: With Internal Microstructure* (Oxford University Press, Oxford, 1994), Vol. 36.
[73] M. James, W. J. T. Bos, and M. Wilczek, Turbulence and turbulent pattern formation in a minimal model for active fluids, Phys. Rev. Fluids **3**, 061101(R) (2018).
[74] X. M. de Wit, M. Fruchart, T. Khain, F. Toschi, and V. Vitelli, Pattern formation by turbulent cascades, Nature (London) **627**, 515 (2024).
[75] H. Xu and Y. Wu, Self-enhanced mobility enables vortex pattern formation in living matter, Nature (London) **627**, 553 (2024).
[76] R. Wang, C. Nisoli, R. Freitas, J. Li, W. McConville, B. Cooley, M. Lund, N. Samarth, C. Leighton, V. Crespi, and P. Schiffer, Artificial 'spin ice' in a geometrically frustrated lattice of nanoscale ferromagnetic islands, Nature (London) **439**, 303 (2006).
[77] R. Chatterjee, N. Rana, R. A. Simha, P. Perlekar, and S. Ramaswamy, Inertia drives a flocking phase transition in viscous active fluids, Phys. Rev. X **11**, 031063 (2021).
[78] B. H. Andersen, J. Renaud, J. Rønning, L. Angheluta, and A. Doostmohammadi, Symmetry-restoring crossover from defect-free to defect-laden turbulence in polar active matter, Phys. Rev. Fluids **8**, 063101 (2023).
[79] A. Doostmohammadi, J. Ignés-Mullol, J. M. Yeomans, and F. Sagués, Active nematics, Nat. Commun. **9**, 3246 (2018).
[80] R. Assante, D. Corbett, D. Marenduzzo, and A. Morozov, Active turbulence and spontaneous phase separation in

inhomogeneous extensile active gels, Soft Matter **19**, 189 (2023).

[81] F. Hecht, New development in freefem++, J. Numer. Math. **20**, 251 (2012).

[82] J. H. W. Lee, J. Peraire, and O. C. Zienkiewicz, The characteristic-Galerkin method for advection-dominated problems—An assessment, Comput. Methods Appl. Mech. Eng. **61**, 359 (1987).